Diacylglycerol kinase promotes actin cytoskeleton remodeling and mechanical forces at the B cell immune synapse

Sara V Merino-Cortés, Sofia R Gardeta, Sara Roman-Garcia, Ana Martínez-Riaño, Judith Pineau, Rosa Liebana, Isabel Merida, Ana-Maria Lennon Dumenil, Paolo Pierobon, Julien Husson, et al.

TITLE

Diacylglycerol kinase ζ regulates actin cytoskeleton remodeling and mechanical forces at the B cell immune synapse

One sentence-summary: Diacylglycerol kinase ζ shapes the B cell response by regulating actin cytoskeleton remodeling, force generation and antigen uptake-related events

Authors

Sara V. Merino-Cortes[1], Sofia R. Gardeta[1], Sara Roman-Garcia[1], Ana Martínez-Riaño[2], Judith Pineau[3], Rosa Liebana[1], Isabel Merida[1], Ana-Maria Lennon Dumenil[3], Paolo Pierobon[3], Julien Husson[4], Balbino Alarcon[2], and Yolanda R. Carrasco[1,*]

Affiliations

[1]Department of Immunology and Oncology, Centro Nacional de Biotecnología (CNB)-CSIC, Madrid, Spain

[2]Department of Cell Biology and Immunology, Centro de Biología Molecular Severo Ochoa (CBMSO), CSIC-UAM, Madrid, Spain

[3]Institut Curie, PSL Research University, INSERM U932, Paris, France

[4]Laboratoire d'Hydrodynamique (LadHyx), Ecole polytechnique, CNRS, Institut Polytechnique de Paris, France

***Corresponding author:** Yolanda R. Carrasco, ycarrasco@cnb.csic.es

Total characters: 83,274 characters

Figures: 6

ABSTRACT

Diacylglycerol kinases (DGK) limit antigen receptor signaling by diacylglycerol consumption in immune cells. The relevance of DGK on phosphatidic acid production in antigen-driven lymphocyte activation and response is unknown. Here we showed that DGKζ isoform regulates LFA-1-mediated adhesion and F-actin content at the B cell immune synapse mainly by phosphatidic acid. Measurement of single-cell mechanical force generation indicated that DGKζ-deficient B cells exert lower forces at the synapse than wild-type. Non-muscle myosin activation and MTOC translocation to the synapse were also impaired. These functional defects correlated with decreased B cell ability to present antigen and activate T cells in vitro. The in vivo germinal center response of DGKζ-deficient B cells was also reduced, indicative of a disadvantage to compete for T cell help. Altogether, our data demonstrate that DGKζ shapes B cell responses by regulating actin remodeling, force generation and antigen uptake-related events at the immune synapse. Hence, an appropriate diacylglycerol/phosphatidic acid balance is required for optimal B cell function.

INTRODUCTION

Diacylglycerol kinases (DGK) convert lipid diacylglycerol (DAG) into phosphatidic acid (PA), shaping the pool of both second messengers. There are ten mammalian DGK isoforms classified in five subgroups based on distinct regulatory domains. They are soluble enzymes that translocate to specific cellular locations to regulate the DAG/PA levels (reviewed at (*1*), (*2*)). Enrichment of DAG or PA at the plasma membrane supports the localized recruitment of protein effectors. DAG-dependent effectors include conventional PKC, PKD and RasGRP, which drive the activation of NFκB and ERK1/2 signaling cascades, and finally gene transcription. PA acts as a lipid anchor for distinct effectors through the binding of its negative charge to cationic regions on those proteins. PA-binding proteins, as the Rac activator DOCK1, RhoGDI or atypical PKCζ and Par3, are involved in cytoskeletal remodeling and cell polarity (reviewed at (*1*), (*2*)).

In immune cells, DGK are well-known for limiting the intensity of DAG-regulated signals downstream of antigen stimulation. DGKα and DGKζ are the most studied isoforms, both expressed in B and T cells (*1, 3*). Antigen recognition on the surface of antigen-presenting cells (APC) triggers the formation of the immune synapse (IS) at the lymphocyte/APC interface. IS establishment requires actin cytoskeleton remodeling and protein segregation in two concentric domains: the central supramolecular activation cluster (cSMAC), which is characterized by central accumulation of antigen/antigen-receptor together with certain signaling molecules; and the peripheral ring-shaped domain (peripheral SMAC, pSMAC), which is enriched in LFA-1/ICAM-1 adhesion molecules, filamentous actin (F-actin) and other proteins involved in adhesion and cytoskeletal rearrangements (vinculin, talin, WASP) (*4-7*). In T cells, PLCγ generates a localized DAG pool at the IS to trigger downstream signaling (*8*); both DGKα and DGKζ translocate to the IS to regulate DAG levels, thus impacting TCR-signaling intensity (*9, 10*). DGKζ-

deficient B cells showed enhanced Ras-ERK1/2 pathway activation after BCR stimulation, leading to increased B cell responses (*3*).

In non-immune cells, DGK participate in actin cytoskeleton rearrangements, cell polarity and integrin recycling. DGKα-mediated PA generation at the plasma membrane recruits PKCζ, which phosphorylates RhoGDI. This promotes the release and activation of Rac1 and thus, actin polymerization for invasive protrusion generation in epithelial cells (*11*). Similarly, DGKζ-produced PA facilitates Rac1 activation by PAK1-mediated phosphorylation of RhoGDI in neuronal and skeletal muscle cells (*12, 13*). PA generation by DGK regulates integrin recycling and tumor invasiveness by the Rab11-dependent pathway (*14*). PA also targets PIP5KI, promoting its lipid kinase activity to produce PIP_2 at the plasma membrane (*15, 16*); PIP_2 is substrate for PLCγ and PI3K, and regulates adhesion and actin dynamics (*17*). Actomyosin reorganization, integrin clustering and polarized membrane trafficking happen at the IS. DGK are linked to T cell polarization events, as MTOC translocation and polarized secretion at the IS are impaired in absence of DGKα or DGKζ (*18, 19*). Nonetheless, the PA-related DGK functions at the IS are largely unknown.

Here we investigated the role of DGK in B cell synapse assembly. We used mouse primary B cells deficient of DGKζ ($DGK\zeta^{-/-}$), DGKα ($DGK\alpha^{-/-}$) or treated with a DGK kinase inhibitor. In addition, we employed a B cell line overexpressing GFP-tagged DGKζ constructs. We found that DGKζ regulates LFA-1-mediated adhesion and F-actin accumulation at the IS mainly through PA generation, and that DOCK2/PAK1 regulation of Rac activity was also involved. Furthermore, we employed Traction Force Microscopy (TFM) and Micropipette Force Probe (MFP) to study single-cell force generation at the IS (*20, 21*). We detected decreased mechanical forces for $DGK\zeta^{-/-}$ and inhibitor-treated B cells. Forces are critical to acquire antigen at the B cell IS (*22*). These results together

with impaired myosin activation and MTOC translocation to the IS correlated with the diminished ability of DGKζ-defective B cells for antigen extraction and presentation to T cells in vitro. In immunocompetent mice, DGK$\zeta^{-/-}$ B cells exhibited reduced germinal center (GC) responses. Our data demonstrate pivotal functions for DGKζ in cytoskeletal remodeling, mechanical forces and antigen uptake at the IS to govern B cell responses.

RESULTS

DGKζ regulates LFA-1-adhesion and F-actin accumulation at the B cell IS

We analyzed protein expression of DGKα and DGKζ in B cells by immunoblot. Both isoforms were detected in wild-type (WT) B cells, which is in line with previous findings at the RNA level (*3*). Treatment with the DGK inhibitor R59949 (R59-treated) had no significant effect on DGKα/ζ levels (fig. S1A). We investigated the ability of DGKζ$^{-/-}$, DGKα$^{-/-}$ or R59-treated B cells to trigger IS formation and maturation compared to WT. For inhibitor experiments, B cells were pre-treated with R59 (10 μM, 30 min at 37ºC) and washed before use. We used artificial planar lipid bilayers that contained GPI-linked ICAM-1 adhesion molecule, CXCL13 chemokine coating and various densities of tethered surrogate antigen (anti-κ LC antibody; su-Ag). This system mimics an APC surface and was used to evaluate synapse formation by confocal microscopy (*4*). Splenic B cells were isolated by negative selection (<90% CD19^{+}); WT and DGKζ$^{-/-}$ B cells showed similar IgM/IgD surface expression, while DGKα$^{-/-}$ B cells displayed slightly higher IgM levels (fig. S1B and C). B cells were left in contact with the lipid bilayer (10 min at 37ºC), and then imaged. The frequency of B cells able to establish the IS was analyzed based on two criteria: the formation of a central su-Ag cluster (cSMAC), and of a cell contact with the substrate (IS contact area), which were estimated by su-Ag-associated fluorescence and by interference reflection microscopy (IRM), respectively. At 20 molecules (molec)/μm^2 su-Ag density, we found a small increase in IS formation frequencies for DGKζ$^{-/-}$ B cells compared to controls; R59-treated B cells showed a similar tendency (Fig. 1A and B). In IS-forming B cells, contact areas (estimated by IRM) were significantly diminished in DGKζ$^{-/-}$ and R59-treated B cells (Fig. 1C and D). In contrast, the area and the total quantity of su-Ag accumulated at the IS (both estimated by fluorescence) were comparable between DGKζ$^{-/-}$, R59-treated and WT B cells (Fig.

1C and D). Similar results were obtained when using lower su-Ag densities at the lipid bilayer (fig. S1D-I). As the contact area is the sum of su-Ag central cluster area (cSMAC) and the surrounding LFA-1/ICAM-1 interactions (pSMAC), these data implied that impaired DGKζ function caused pSMAC defects. We analyzed other pSMAC features, namely vinculin and F-actin content at the lipid bilayers by immunofluorescence. DGKζ$^{-/-}$ B cells had less vinculin and F-actin at the pSMAC than controls with the su-Ag densities tested; the reductions were stronger for R59-treated B cells (Fig. 1E-H). In contrast, DGKα$^{-/-}$ B cells showed unimpaired IS formation (pSMAC/cSMAC; vinculin/F-actin content) (fig. S2). We then centered our study in the DGKζ isoform; lack of DGKζ did not change DGKα protein levels (fig. S1A). We also determined that a su-Ag density of 20 molec/μm^2 was optimal and was employed in subsequent IS formation analyses.

We set out to study the effect of an excess of DGKζ activity on IS formation. A20 B cells were transiently transfected with GFP-tagged constructs for DGKζ-WT or kinase dead mutant (DGKζ-KD). GFP-transfected and none-transfected (GFP^{neg}) A20 cells were included as controls (fig. S3A). Using the aforementioned experimental approach, we found that both DGKζ constructs decreased the frequency of IS formation (fig. S3B and C). The IS contact areas were bigger, while there were no differences in su-Ag cluster area or total quantity (fig. S3D and E). By IF, we detected significantly enhanced F-actin content at the pSMAC of A20 B cells overexpressing DGKζ-WT but not for DGKζ-KD (fig. S3F). For vinculin, we observed increased frequency of A20 cells with a well-formed ring as well as enhanced vinculin content in cells overexpressing DGKζ-WT or DGKζ-KD (fig. S3G). Data thus indicated a role for DGKζ in regulating LFA-1-adhesion, vinculin recruitment and F-actin content at the B cell IS.

DGKζ-derived PA shapes LFA-1-adhesion and the DOCK2/Rac/F-actin molecular axis at the B cell IS

We next investigated if an excess of PA could rescue the defects in LFA-1 adhesion and F-actin caused by impaired DGKζ function. To do so, we left WT and DGKζ$^{-/-}$ B cells, untreated or treated with R59, to form the IS and then added exogenous PA (0.1 mM) to the medium. After 30 min of PA exposure, we imaged the cells and detected bigger IS contact areas in all instances (Fig. 2A and B). The su-Ag area values and total quantity at the IS were lower after PA treatment (fig. S4A and B). By IF, we detected increased F-actin content at the synapse of PA-exposed B cells (Fig. 2C and D). Boosting PA levels then resulted in enhanced LFA-1 adhesion and actin polymerization at the IS; su-Ag central cluster dynamics was also altered.

Previous studies noted the relevance of PI3K-derived PIP_3 to regulate the F-actin ring assembly at the T cell IS. PIP_3 recruits DOCK2 to the periphery of the synapse, which promotes actin polymerization through the Rac GTPases (*23*). We addressed the interplay between PIP_3 and DGKζ-derived PA in B cell IS formation. PI3K activity in WT and DGKζ-impaired (knockout and R59-treated) B cells was assessed by measuring Akt phosphorylation after BCR stimulation with anti-mouse IgM antibody (Ab)-coated plates; we found no significant differences between the three cell types (fig. S5A). We treated WT and DGKζ$^{-/-}$ B cells with the PI3K inhibitor LY294002 (LY; 10 μM, 30 min at 37ºC), and then settled them on the lipid bilayers for IS formation. LY-treatment caused a reduction in IS area but also in su-Ag cluster size in both cell types (fig. S5B-D); F-actin content was also affected (Fig. 2E). Within Class I PI3K, the PI3Kδ isoform (p110δ catalytic subunit) was identified as the major contributor for PIP_3 production to regulate F-actin remodeling at the IS (*23*). We isolated splenic B cells from knock-in mice expressing a kinase-dead p110δ catalytic subunit (PI3Kδ KD), treated them or not with

R59, and evaluated IS formation. PI3Kδ KD B cells displayed lower IS contact area and F-actin content than controls (fig. S5E and F; Fig. 2F); we also detected increased su-Ag aggregation in PI3Kδ KD B cells (fig. S5E and G). R59 treatment of PI3Kδ KD B cells decreased even more IS area and F-actin content compared to untreated cells, without modifying su-Ag clustering (fig. S5E-G; Fig. 2F).

We studied DOCK2 recruitment to the IS in splenic B cells isolated from DOCK2-GFP knock-in mice, untreated or treated with R59. We observed a ring-shape DOCK2-GFP structure at the IS; quantification of total DOCK2-GFP fluorescence at the IS plane revealed a significant reduction when B cells had been treated with R59 (Fig. 2G). DGKζ-dependent PAK1 activation promotes RhoGDI/Rac dissociation and thus Rac activation (*24*). We analyzed active PAK1/2 (phosphorylated PAK1/2; p-PAK1/2) by immunoblot; DGKζ$^{-/-}$ and R59-treated B cells had lower p-PAK1/2 levels than controls, while DGKζ-WT overexpression in A20 B cells increased p-PAK1/2 levels (Fig. 2H). PA exposure did not enhance p-PAK1/2 content in WT B cells (fig. S4C). This suggests that DGKζ associates with PAK/RhoGDI complex and promotes its activation, as described in fibroblasts (*24*). Hence, our data suggest that DGKζ regulates actin polymerization at the B cell IS by affecting Rac function by DOCK2 and PAK1/2.

DGKζ regulates mechanical forces at the B cell IS

Several studies revealed the relevance of mechanical forces at the IS for B and T cell effector function (reviewed at (*20*), (*25*)). The robust actin polymerization and remodeling at the IS induces force generation. LFA-1 and antigen receptors act as mechanosensitive proteins because their function and signaling properties are shaped by those mechanical forces. DGKζ$^{-/-}$ and R59-treated B cells had defects in LFA-1 adhesion and F-actin levels at the IS. We asked whether that affected the mechanical forces generated at the synapse

of those B cells compared to WT. To do that, we employed two complementary methods: TFM and MFP. We measured the forces exerted by B cells when in contact with polyacrylamide hydrogels loaded with su-Ag alone, or in combination with ICAM-1-Fc, by TFM. Displacements of the fluorescent microbeads embedded on the hydrogel, monitored over time, allow to calculate the applied forces magnitude (fig. S6A) and the cell strength on the substrate at each time point. Traction energy values were significantly higher in presence of ICAM-1 at the substrate compared to su-Ag alone (Fig. 3A and B; Movies 1 and 3), pointing to the importance of LFA-1 adhesion for synaptic force generation. DGK$\zeta^{-/-}$ B cells exhibited reduced traction forces compared to controls in presence of su-Ag plus ICAM-1 (Fig. 3A and B; Movies 2 and 4).

To define the three-dimensional components of the forces, we deliniated the B cell mechanical behavior and quantified the forces generated at the IS over time by MFP (*21*). In this technical approach, a bead coated with stimulatory ligands is aspirated at the tip of a flexible micropipette used as a sensitive force transducer, and brought in contact with the cell, aspirated at another micropipette's tip (fig. S6B). We used silica beads (5 μm diameter) coated with lipid bilayers containing GPI-ICAM-1 and tethered su-Ag. After contact with the stimulatory bead, WT B cells pushed it away during the first 40 sec (positive values of bead displacement, X_{bead}, relative to initial bead position) (Fig. 3C and D; Fig. S6C; Movies 5 and 6) at a pushing speed of 0.025±0.010 μm/sec (Fig. 3E). DGK$\zeta^{-/-}$ B cells showed a reduced pushing phase that correlated with lower pushing speed values (0.015±0.005 μm/sec; Fig. 3C-E; Movie 7). Then, WT B cells pulled the bead (X_{bead} reached negative values) and formed a cup-like structure on it (Fig. 3C and D; Fig. S6C; Movie 6); pulling ability was diminished in DGK$\zeta^{-/-}$ B cells (Fig. 3D). MFP also allows the measurement of cell rigidity just upon cell contact with the bead, before the pushing phase begins (Young's modulus parameter) (*21*); values were higher with su-Ag

compared to non-antigen (Fig. 3F), indicating increased cell-stiffness after BCR stimulation. Young's modulus values for DGKζ$^{-/-}$ B cells were lower than for WT in presence of su-Ag (Fig. 3F). In order to measure cell mechanical changes at the IS, we monitored B cell elastic properties by quantifying cell stiffness through the *K*' parameter. Compared to WT, DGKζ$^{-/-}$ B cells had lower *K*' values (Fig. 3G); this indicated impaired ability for cytoskeleton remodeling, which changed their mechanical properties on IS formation. Likewise, we detected mechanical defects in R59-treated B cells (Fig. 3 H-J; Movie 8). Therefore, data obtained from both TFM and MFP suggest that DGKζ governs mechanical properties and force generation at the B cell IS.

DGKζ activity limits IS-triggered B cell activation

A previous study reported that lack of DGKζ enhances activation of DAG-dependent pathways upon B cell stimulation, in vitro, with soluble antigen; ERK1/2 activation, CD69 expression and cell proliferation increased (*3*). We investigated the effects of DGKζ-impaired function for B cell activation in regard to the IS. We loaded WT, DGKζ$^{-/-}$ and R59-treated B cells with a Ca^{2+}-sensitive fluorescent probe, and monitored Ca^{2+} influx during synapse formation by real time fluorescence microscopy. The peak and sustained Ca^{2+} influx was enhanced in DGKζ$^{-/-}$ and R59-treated B cells compared to controls (Fig. 4A and B); this might be due to increased stimulation of DAG-dependent Ca^{2+} channels (*26*). We evaluated ERK1/2 activation (phosphorylated ERK1/2; p-ERK) at the synapse by immunofluorescence (Fig. 4C); DGKζ absence or kinase inhibition resulted in higher p-ERK (Fig. 4D). DGKζ$^{-/-}$ B cells showed similar p-ERK levels at the IS than R59-treated WT. This supports the major role of DGKζ isoform in limiting DAG-related signaling downstream the BCR, as previously reported (*3*); indeed, lack of DGKα did not modify p-ERK levels at the B cell IS compared to WT (fig. S6D). The increased

p-ERK levels in R59-treated DGKζ$^{-/-}$ B cells compared to untreated ones implies the contribution of another DGK isoform in absence of DGKζ.

We incubated B cells in contact with planar lipid bilayers, unloaded or su-Ag loaded, for 20 h and then analyzed the surface expression of CD69, CD25 and CD86 activation markers by flow cytometry. DGKζ$^{-/-}$ B cells expressed higher level of those markers than WT, although the increase was statistically significant only for CD69; R59-treatment had a similar effect (Fig. 4E and F). In order to evaluate cell proliferation, we modified the experimental approach (fig. S7A); we used silica beads (5 μm diameter) coated with lipid bilayers containing GPI-ICAM-1, CXCL13 coating and tethered su-Ag, as they were suitable for longer co-culture periods. We named them as pseudo-APC. We increased su-Ag density (1000 molecules/μm^2) at the pseudo-APC surface to promote greater B cell proliferation, thus facilitating detection. WT, DGKζ$^{-/-}$ and R59-treated B cells were CFSE-stained and co-cultured with pseudo-APC at different ratios (1:1, 1:5) in presence of IL-4 for 96 h. Compared to WT, DGKζ$^{-/-}$ B cells showed increased proliferation although R59-treatment did not alter it (Fig. 4G and H; gating strategy shown in fig. S7A).

DGKζ deficiency diminishes B cell antigen-presentation capacity in vitro

B cell immunity against T-cell dependent antigens entails antigen acquisition, degradation and presentation to T cells in the form of antigenic peptides by the MHC class-II complex. In this process, B cells receive T cell help, mainly through CD40 stimulation, which triggers B cell survival, proliferation and class-switching. We investigated the DGKζ role in molecular events related to antigen acquisition, processing and presentation. MTOC polarization to the IS supports the membrane trafficking needed for those events (*27*). We incubated WT, DGKζ$^{-/-}$ and R59-treated B cells with pseudo-APC, unloaded or loaded with su-Ag, at a ratio of 1:1 for 30 min at 37ºC, then fixed them

and analyzed MTOC location by γ-tubulin staining. MTOC distance to the IS for each B cell was measured and normalized to the cell diameter. Su-Ag promoted MTOC relocation in most WT B cells (70%); DGKζ dysfunction significantly decreased it (20% in DGKζ$^{-/-}$; 30% in R59-treated) (Fig. 5A and B). The non-muscle motor protein myosin-II is involved in antigen extraction at the B cell IS (*22*). Therefore, we analyzed phosphorylation of the regulatory subunit myosin light chain (MLC) after BCR triggering with Ab-coated plates by immunoblot; DGKζ$^{-/-}$ and R59-treated B cells had impaired MLC activation compared to controls (Fig. 5C).

We evaluated B cell antigen extraction and presentation to T cells in vitro. We prepared GPI-ICAM-1/CXCL13-containing planar lipid bilayers unloaded or loaded with a mixture of su-Ag and Alexa Fluor 488-conjugated ovalbumin protein (OVA; see methods). To quantify BCR-mediated antigen extraction, we measured the fluorescence of the Alexa Fluor 647-conjugated streptavidin (strep) used to tether su-Ag/OVA to the lipid bilayer (see methods); OVA acquisition was also monitored through Alexa Fluor 488 fluorescence detection. We incubated WT B cells in absence or presence of su-Ag/OVA at different densities (ranging from 20 to 2500 molec/μm^2) for 2 h at 37ºC, collected them, trypsin-treated and analyzed by flow cytometry. We were able to detect strep/OVA extraction at 500 and 2500 molec/μm^2 densities (~30% and 70% strep$^+$ B cells, respectively), and was fully dependent on BCR-stimulation by tethered su-Ag (fig. S7B). We then evaluated antigen extraction ability of DGKζ$^{-/-}$ and R59-treated B cells using the highest density to improve strep detection. Strep$^+$ B cell frequencies were similar but mean fluorescence intensity values were lower for DGKζ$^{-/-}$ and R59-treated B cells than for WT; this indicates reduced antigen acquisition although the difference was not statistically significant (Fig. 5D and E). Exogenous PA addition did not modify antigen extraction ability of WT B cells (fig. S7C).

To assess T cell antigen presentation, we incubated WT, DGKζ$^{-/-}$ and R59-treated B cells in contact with unloaded or su-Ag/OVA-loaded planar lipid bilayers (2 h, 37ºC). B cells were then collected and co-cultured with CFSE-labeled OT-II CD4^{+} T cells at a 1:1 ratio (fig. S7D). The TCR of OT-II CD4^{+} T cells recognizes OVA 323-339 derived-peptides in the context of MHC class-II (I-A^{b}) on the B cell surface, triggering T cell activation. After 72 h, we evaluated CD25 surface expression as T cell activation marker, T cell proliferation (gating strategy shown in fig. S7D) and IL-2 levels in the supernatants. Using this system, we detected increased CD4^{+} CD25^{+} T cell frequencies (up to 25%) in presence of su-Ag/OVA compared to the control condition for WT B cells; frequency values were significantly reduced for DGKζ$^{-/-}$ and R59-treated B cells (Fig. 5F and G). T cell proliferation and IL-2 production were reduced when using DGKζ$^{-/-}$ or R59-treated B cells (Fig. 5F, H and I). These results indicate that DGKζ affects antigen presentation by regulating antigen acquisition/processing-related molecular events at the IS.

Absence of DGKζ in B cells impaired the GC response in vivo

We investigated if the antigen presentation defects found in B cells with altered DGKζ function limited GC responses to T-dependent antigens in vivo. We isolated WT or DGKζ$^{-/-}$ B cells (CD45.2^{+}) and adoptively transferred them to CD45.1^{+} immunocompetent recipient mice. One day later mice were immunized with NIP-OVA embedded in Alum, and the splenic GC response was evaluated at day 7 post-immunization by flow cytometry. We followed the gating strategy depicted in Fig. 6A for CD45.2^{+} B cell analysis. The frequency of NP-specific GC (GL7^{+} Fas^{+} NP^{+}) B cells was significantly lower in mice transferred with DGKζ$^{-/-}$ compared to those transferred with WT B cells (Fig. 6B and C). We determined the frequency of plasma cells (PC; CD138^{+}) and IgG1^{+} B cells within the CD45.2^{+} B cell population; transferred DGKζ$^{-/-}$ B

cells showed reduced frequencies of both populations in comparison to controls (Fig. 6D and E). Transferred DGK$\zeta^{-/-}$ B cells had preferential generation of IgM^{+} PC *versus* IgG1^{+} PC as compared to WT (Fig. 6F and G). The memory-like CD138^{-} IgG1^{+} B cell subset was lowered for DGK$\zeta^{-/-}$ than for WT B cells, although not statistically significant. As expected, the recipient CD45.1^{+} B cell response was comparable between animals transferred with CD45.2^{+} WT B cells or CD45.2^{+} DGK$\zeta^{-/-}$ B cells (fig. S8). These results evidence that DGK$\zeta^{-/-}$ B cells have a competitive disadvantage for T cell help, which results in diminished GC responses.

DISCUSSION

This study reports a pivotal role for DGKζ in the regulation of actin polymerization and LFA-1-mediated adhesion at the B cell IS and, consequently, in the generation of mechanical forces at the synapse. Impaired MTOC translocation to the IS also suggests that DGKζ regulates cell polarity-related events in this context. Traction forces and cell polarization are necessary for antigen acquisition and processing at the B cell synapse (*22, 28, 29*). The B cell ability to present antigenic peptides determines the chances of receiving co-stimulatory T cell help and subsequent fate of the B cell response. Data from in vitro and in vivo assays support a role for DGKζ in shaping B cell ability to extract antigen from the APC surface, and thus to get T cell help and succeed in the GC.

IS formation induces robust actin polymerization and the assembly of a peripheral F-actin ring, which provides a framework for signaling events, membrane trafficking, and adhesion support. In T cells, PI3K-mediated PIP_3 production at the synapse periphery plays a major role in the F-actin ring maintenance (*23*). PIP_3 recruits DOCK2, promoting Rac activation, and thus, actin polymerization. Our data support a similar role for PIP_3 in regulating F-actin ring formation at the B cell synapse. Besides, DGKζ$^{-/-}$ B cells and DGK-inhibited WT or PI3Kδ KD B cells showed reduced F-actin levels at the IS, whereas PA exposure and DGKζ overexpression increased the size and content of the F-actin ring. DGKζ and its product, PA, are thereby involved in the regulation of F-actin ring formation at the B cell IS. Previous reports in non-immune cells showed the DGKζ relevance to connect lipid signaling with actin reorganization through its kinase and scaffold activities. DGKζ associates with the PAK1/RhoGDI/Rac1 complex and promotes Rac activation; both scaffold and kinase functions are needed (*24*). DGKζ also regulates RhoA activation by a scaffolding mechanism, forming a complex with PKCα/RhoGDI (*30*). We propose that DGKζ affects Rac function and actin

polymerization at the IS by regulating DOCK2 recruitment and PAK1/2 activation. Our data with the KD construct, the exogenous PA addition and the reduction of DOCK2-GFP levels in R59-treated B cells evidence a major contribution of DGKζ kinase activity. Additionally, the lack of p-PAK1/2 induction upon PA exposure suggests the involvement of DGKζ scaffold properties. PAK1/2 are also targets of active Rac and able to coordinate actin cytoskeleton remodeling (*31, 32*); their implication in IS assembly downstream of Rac needs of further studies. In neutrophil migration, DOCK2 dynamics at the plasma membrane is sequentially regulated by PIP_3 and PA; upon stimulation, PIP_3 rapidly recruits DOCK2 to the plasma membrane, while PA generation stabilizes DOCK2 at the membrane promoting its local accumulation and Rac activation (*33*). We propose that, in a similar fashion, sequential PIP_3/PA action governs DOCK2 dynamics and thus F-actin ring maintenance at the B cell IS. BCR signaling initially leads to PI3K activation and PIP_3 production; PLCγ2-mediated PIP_3 degradation produces DAG that activates classical PKC; PKC phosphorylates DGKζ driving its activation and relocation to the plasma membrane, where it produces PA (fig. S9).

DGKζ$^{-/-}$ and R59-treated B cells presented increased BCR-triggered Ca^{2+} influx. Ca^{2+} influx downstream of the BCR is mainly driven by PLCγ2/IP_3-dependent activation of store-operated Ca^{2+} channels (SOCs). Nonetheless, B cells express several members of the Ca^{2+}-permeable transient receptor potential channels (TRPC) (*34*). TRPC activation seems to be Ca^{2+}-store-independent and DAG-sensitive (*35-37*). Previous work in the DT40 B cell line showed that DAG-dependent Ca^{2+} influx by TRPC3 enhances Ca^{2+} signaling downstream the BCR; TRPC3 promotes PLCγ2 translocation to the plasma membrane and activation, maintaining IP_3 and DAG production (*26, 38*). Besides, active TRPC3 retains PKCβ at the plasma membrane by direct interaction, that sustains ERK1/2

activation (*26*). The lack of DGKζ activity allows DAG accumulation, that might amplify Ca^{2+} influx and signaling downstream the BCR by inducing TRPC3 activation.

Cell polarization at the B cell IS orchestrates the membrane trafficking events required for antigen processing and presentation to T cells. MHC class-II-containing lysosomes translocate together with the MTOC to the synapse, where their local secretions promote antigen extraction (*29*). MTOC/lysosomes polarization is regulated by the Cdc42 GTPase and its effector, the atypical PKCζ, being the latter part of the Par polarity complex together with Par3 and Par6 (*29*). Par3 is enriched at the B cell IS and involved in MTOC/lysosomes transport to the synapse interface (*39*). DGK-derived PA regulates PKCζ location and activity in non-immune cells (*11*). In DGKζ$^{-/-}$ OTI CD8^{+} cytotoxic T cells, impaired MTOC recruitment to the IS correlated with lower active (phosphorylated)-PKCζ levels at the synapse interface (*18*). DAG accumulates at the CD4^{+} T cell IS and establishes an intracellular gradient that drives MTOC polarization; three novel PKC (ε, η, θ) and the motor protein dynein are involved (*40, 41*). DGKα has a major role in shaping the DAG gradient at the synapse and establishing T cell polarity (*19*). A recent report showed that Arp2/3-dependent F-actin nucleation at the MTOC connects this organelle with the nucleus in resting B cells; BCR stimulation reduces F-actin content at the MTOC allowing its detachment from the nucleus and polarization to the IS (*42*). The defects in MTOC translocation of DGKζ$^{-/-}$ and DGK-inhibited B cells suggest that DGKζ promotes cell polarization events. More studies are necessary to relate DGKζ with the PKCζ/Par3 axis, F-actin nucleation at the MTOC or the DAG-gradient in B cells.

Actin cytoskeleton remodeling drives force generation in cells; actin polymerization *per se* creates pushing forces while F-actin, in combination with myosin II contractile activity, produce pulling forces. To generate and exert forces against the extracellular

matrix, or another cell, cells connect protrusive/contractile F-actin dynamics to adhesion structures (reviewed at (*43*)). Lymphocytes link actin dynamics to the LFA-1-mediated adhesion at the IS; vinculin and talin are involved in that. Our data point to DGKζ as a regulator of force generation at the B cell IS; this may be achieved by influencing LFA-1-mediated adhesion, actin polymerization and myosin II activity downstream of the BCR. In T cells, F-actin flow and mechanical forces are important for LFA-1 activity at the IS (*44*). DGKζ might affect LFA-1-mediated adhesion through Rac and/or myosin activities. Also, DGK-produced PA promotes PIP5KI activity and subsequent PIP_2 generation; PIP_2 recruits to the plasma membrane proteins involved in actin polymerization and adhesion site dynamics, as vinculin, talin and WASP (*4, 17, 45*). Though more investigations are required to dissect the underlying mechanisms, DGKζ appears to employ the molecular axis DOCK2-PAK1/Rac and PIP5K/PIP_2 to regulate mechanical force generation at the IS. Our studies using the MFP technique showed a sequential pushing/pulling/cup-like stages during B cell IS formation, alike T cells (*21, 46*). Inhibitor treatments in T cells indicated a main role of the actin cytoskeleton for the pushing forces, while myosin activity was needed for the pulling/contractile stage; PI3K-DOCK2 signaling also participates of the pulling phase (*47*). The lower pushing and pulling forces values in DGK$\zeta^{-/-}$ B cells correlated with impaired actin polymerization at the IS and myosin activation.

Two mutually non-exclusive mechanisms support antigen acquisition from the APC surface by B cells: local secretion of lysosomes at the IS interface, which liberates proteases to facilitate antigen extraction (*29*), and myosin-II mediated pulling forces that promote antigen/BCR complexes internalization (*22*). Myosin-II-derived forces allow discrimination of BCR affinity for the antigen, crucial for the T cell-dependent selection of high affinity GC B cells (*28*). Our results suggest that DGKζ-mediated regulation of

mechanical forces and MTOC translocation at the B cell IS facilitates antigen acquisition and presentation to T cells. In our in vitro system, OVA co-exists with su-Ag at the planar lipid bilayer without being physically attached to each other; this implies that lysosomal secretion and/or strong forces able to detach a piece of artificial membrane are required for OVA acquisition and degradation.

In a competitive in vivo environment, we demonstrated that lack of DGKζ resulted in reduced GC B cell activity, diminished numbers of antigen-specific GC B cells, PC and IgG1 class-switched B cells. A previous study addressed the DGKζ role in the B cell response by immunization of DGKζ$^{-/-}$ mice with NP-Ficoll, a T-independent type 2 antigen (*3*). This study reported higher antigen-specific IgM/IgG3-secreting PC and IgM/IgG3 serum levels in DGKζ$^{-/-}$ compared to WT mice, suggesting that DGKζ limits the early PC response. In addition, they used MD4 BCR (HEL-specific) transgenic B cells, WT (CD45.1) and DGKζ$^{-/-}$ (CD45.2) mixed at 1:1 ratio, to adoptively transfer immunocompetent mice. Mice then were immunized with HEL mutants of low and medium affinity conjugated to SRBC, a T cell-dependent antigen. They found increased GC B cell and IgM PC generation for DGKζ$^{-/-}$ B cells compared to WT at the beginning of the antibody response (day 5) (*3*). The model precluded analysis at later time points because MD4 B cells are unable to class-switch. The authors suggested that DGKζ limits early PC generation in T cell-dependent responses by promoting antigen affinity discrimination by DAG signaling. Of note, we evaluated later stages of the GC response; in our system, the reduced IgG1 B cell production, reinforced by the in vitro data on antigen acquisition and presentation, evidence that DGKζ governs B cell ability to acquire antigen and compete for T cell help. Nevertheless, the higher IgM PC frequencies might reflect the enhanced early PC generation for DGKζ-deficient B cells previously described (*3*); in vitro DAG-related activation (Ca^{2+} influx, ERK1/2, CD69/CD25/CD86

upregulation) and proliferation in DGK$\zeta^{-/-}$ B cells were enhanced compared to those in WT after BCR stimulation, as also reported in that study (*3*). The later timing of analysis and impaired ability for getting T cell help might account for the reduced GC frequencies in our model compared to the previous study. B cell 1clone frequency and antigen affinity determine B cell recruitment to and interclonal competition at the GC (*48*). The affinity values reported for HEL^{3X} (low affinity mutant) and NP are similar ($K_D \sim \mu M$ range), but distinct B cell precursor frequency might also explain the differences in results. B cell competition for antigen is likely lower in the previous model than in ours, as all (and only) the transferred B cells recognize the antigen (HEL) used for immunization; that is not the case in our experimental approach. The way of antigen administration (NIP-OVA in Alum *versus* HEL on SRBC) may have also accounted for some of the differences.

DGK are currently consider as therapeutic targets to manipulate T cell function in autoimmune diseases and to subvert tumor immunosuppression. Increased DGKα and DGKζ expression correlate with reduced effector function in tumor-infiltrating lymphocytes (TIL) (*49, 50*). The pharmacological intervention of DGK focuses on their capacity to limit DAG-mediated signals and subsequent gene transcription. Our study underlines the relevance of DGKζ functions pertaining to PA generation for B cell function. The described roles for DGKζ in organizing the B cell:APC communication platform might also apply to other immune cell interactions and should be considered when targeting DGK for therapeutic intervention.

METHODS

Mice and B cell isolation

Primary B lymphocytes were isolated from spleens of adult (10- to 20-week-old) WT, DGK$\zeta^{-/-}$ (*51*), DGK$\alpha^{-/-}$ (*52*), PI3Kδ kinase dead (provided by D.F. Barber, CNB-CSIC, Spain; (*53*)) and DOCK2-GFP knock-in (provided by J. Stein, University of Bern, Switzerland, and Y. Fukui, Kyushu University, Japan; (*54*)) mice, all of them in C57BL/6 genetic background. Splenic B cells were purified by negative selection using mouse pan-T Dynabeads (DynaI Biotech, Invitrogen) after a Lympholyte step (Cedarlane Laboratories); we enriched to >90% B cells. Primary OTII $CD4^+$ T cells were isolated from the spleen of adult OTII transgenic (OVA 323-339-specific TCR) mice (*55*) by negative selection, using a $CD4^+$ T cell isolation kit (MACS, Miltenyi Biotec; purity > 90% $CD4^+$ T cells). Animal procedures were approved by the CNB-CSIC Bioethics Committee and conform to institutional, national and EU regulations. The A20 mouse B cell line was transiently transfected with plasmids encoding for GFP or cherry fluorescent protein alone, GFP- or cherry-DGKζ-WT or -DGKζ-kinase dead (KD) constructs (*9*) by electroporation (260 mV, 950 μF) and used 20 h after transfection. Cells were cultured in complete RPMI (10 mM Hepes, 2 mM L-Glu and 50 μM β-mercaptoethanol) supplemented with 10% FCS.

Real-time microscopy on planar lipid bilayers

Artificial planar lipid bilayers were assembled in FCS2 chambers (Bioptechs) as described (*56*). Briefly, unlabeled murine GPI-linked ICAM-1-containing 1,2-dioleoyl-PC (DOPC) liposomes and DOPC liposomes containing biotinylated lipids were mixed with DOPC liposomes at distinct ratios to obtain specified molecular densities (ICAM-1 at 200 molecules(molec)/μm^2; biotin-lipids, as indicated). Artificial planar lipid bilayers

were assembled on sulphochromic solution-treated coverslips in FCS2 closed flow-chambers (Bioptechs), and blocked with PBS/2% FCS (1 h, room temperature (RT)). Su-Ag was tethered to membranes by incubation with Alexa Fluor 647 or 555 streptavidin (Molecular Probes), followed by monobiotinylated rat anti-κ light chain monoclonal antibody (mAb; clone187.1). Monobiotinylation was achieved labeling the antibody (0.5 mg/ml; 1 ml) with 1 μg/ml NHS-LC-LC-Biotin (30 min, RT, in PBS; Pierce), followed by dialysis and checked by FACS. We estimated the number of molec/μm^2 of GPI-ICAM-1 or anti-κ antibody at the lipid bilayers by immunofluorometric assay using anti-ICAM-1 or anti-rat-IgG antibodies, respectively; we obtained the standard values from microbeads with distinct calibrated IgG-binding capacities (Bangs Laboratories). Before imaging, membranes were coated with murine recombinant CXCL13 (100 nM, Peprotech; 20 min, RT). Lipids stock in chloroform were obtained from Avanti Polar Lipids, Inc.

WT and genetically-modified B cells (4 x 10^6) were co-injected into the warmed chamber (37ºC) for imaging; to distinguish them, one cell type was violet-tracer-labeled (0.1 μM, 10 min, 37ºC; Molecular Probes). When indicated, B cells were pretreated with the pan-DGK inhibitor R59949 (10 μM, 30 min, 37ºC; IC_{50} 3.3 μM; Sigma) or with the PI3K inhibitor LY294002 (10 μM, 30 min, 37ºC; Sigma), and washed before used. Confocal fluorescence (FL) (1 μm-optical section), differential interference contrast (DIC), and IRM images were acquired every 30 s for 10-20 min; consecutive videos were acquired when needed. Similarly, transfected A20 B cells (2 x 10^6) were injected and imaged. For Ca^{2+} flux measurements, B cells were labeled with Fluo-4FF (1 μM, 30 min, RT; Molecular Probes), injected into the warmed FCS2 chamber, and imaged every 10 s for 15 min at low quality to speed up acquisition. Assays were performed in chamber-buffer (PBS, 0.5% FCS, 0.5 g/l D-glucose, 2 mM $MgCl_2$, 0.5 mM $CaCl_2$). For exogenous

PA assays, we used freshly prepared 10 mM PA stock (in 10 mM Tris-HCl pH 8.0, NaCl 150 mM). We left cells in contact with the lipid bilayers for 10 min to form the IS, then we imaged them, and at 15 min time point injected 0.1 mM PA (1 ml) in chamber buffer; after 30 min of PA exposure, B cell were imaged. Images were acquired on an Axiovert LSM 510-META inverted microscope with a 40X oil immersion objective (Zeiss).

Immunofluorescence

Primary B cells or transfected A20 B cells were in contact with ICAM-1/CXCL13 lipid bilayers containing tethered su-Ag for 10 min, fixed with 4% paraformaldehyde (10 min, 37ºC), permeabilized with PBS/0.1% Triton-X100 (5 min, RT), blocked with PBS/2% FCS/2%BSA (overnight, 4ºC), and stained with AlexaFluor 647 phalloidin (Molecular Probes) plus the following antibodies: Rabbit anti-phospho-ERK1/2 (Cell Signaling) plus AlexaFluor 488 goat anti-rabbit IgG (Southern Biotechnology); mouse anti-vinculin (clone hVIN-1; Sigma) plus FITC goat anti-mouse IgG1 (BD Biosciences). For PA assays, B cells were fixed at 30 min after PA exposure and stained for phalloidin as explained. For MTOC analysis, B cells were mixed with unloaded or su-Ag-loaded pseudo-APC (20 molec/μm^2) at 1:1 ratio, cultured for 30 min at 37ºC on poly-L-lysine-coated coverslips, fixed, permeabilized and blocked as above, stained with rabbit anti-γ-tubulin (T5192, Sigma) plus AlexaFluor 488 goat anti-rabbit IgG and mounted using Fluoromount (Southern Biotech). FCS2 chambers and coverslips were imaged by confocal fluorescence microscopy as previously explained.

Cell conjugates and activation assays

For cell activation assays, freshly isolated B cells (2 x 10^5) were co-cultured with unloaded or su-Ag-loaded (20 molec/μm^2) planar lipid bilayers, assembled in glass-

bottom p96-size wells, for 20 h, then collected, and analyzed by flow cytometry. To prepare pseudo-APC, silica beads (5 x 10^6; 5 μm diameter; Bangs Laboratories) were washed in distilled water (5,000 rpm, 1 min, RT), incubated with 20 μl DOPC liposomes containing GPI-linked ICAM-1 (200 molec/μm^2) and biotin-lipids (20 or 1000 molec/μm^2) (10 min, RT), washed twice with chamber-buffer, and then blocked, the su-Ag tethered and coated with CXCL13. For cell proliferation, B cells were labeled with CFSE-tracer (0.1 μM, 10 min, 37ºC), washed with complete RPMI/10% FCS, and co-cultured with unloaded or su-Ag-loaded pseudo-APC at specified ratios and with recombinant murine IL-4 (10 ng/ml, Peprotech), in flat-bottom p96 wells for 96 h. Cells were collected, stained for APC-conjugated CD19, and analyzed for CFSE-tracer dilution in a FACSCalibur cytometer (BD Biosciences).

To assess antigen acquisition and T cell presentation, freshly isolated B cells (5 x 10^5) were cultured for 2 h in contact with ICAM-1/CXCL13 planar lipid bilayers, assembled in glass-bottom p96-size wells; these planar bilayers contained distinct densities of biotinylated lipids (20, 100, 500 or 2500 molec/μm^2), and were loaded with a mixture of monobiotinylated su-Ag (5 μg/ml) and monobiotinylated Alexa Fluor 488-conjugated OVA (Molecular Probes) (10 μg/ml) by previous coating with Alexa Fluor 647-conjugated streptavidin (Molecular Probes). OVA monobiotinylation was performed as explained for su-Ag. B cells were then collected, one-half of them (2.5 x 10^5) treated with trypsin (5 min, 37ºC), washed with complete RPMI/10% FCS, and analyzed by flow cytometry for strep and OVA fluorescence signals to measure antigen extraction. The other half of B cells (2.5 x 10^5) were washed with complete RPMI/10% FCS, and co-cultured with CFSE-tracer labeled $CD4^+$ OTII T cells (2.5 x 10^5) at 1:1 ratio in round-bottom p96 wells. After 72 h, culture supernatant was collected for IL-2 detection by ELISA (kit IL-2 ELISA Max 413005, Biolegend) and cells were collected, stained with

Pacific Blue-conjugated rat anti-mouse B220, APC-conjugated rat anti-mouse CD4 and PE-Cy7-conjugated rat anti-mouse CD25, and analyzed for CFSE-tracer dilution and CD25 expression in the $CD4^+$ T cell population in a FACS LSR-II cytometer (BD Biosciences). When required, B cells were pretreated with R59 inhibitor 30 min before adding them to the planar lipid bilayers; the inhibitor was kept during the antigen extraction time (2 h). When indicated, B cells were exposed to 0.1 mM PA for the 2 h of antigen extraction.

Imaging data analysis

The frequency of IS formation per imaged field was estimated as [nº of B cells showing a central su-Ag cluster and IRM contact / total nº of B cells (estimated by DIC)] x 100, using FiJi (NIH) software. 1-μm-optical section confocal images were acquired at the contact plane/IS plane; we used the IRM confocal image to focus on the B cell/artificial membrane contact plane and to define the IS plane. Imaris 7.0 software (Bitplane) was used for qualitative and quantitative analysis of FL signals, as well as for cell contact area (IRM area) and su-Ag cluster area measurements. To set up the background of FL intensity signal, we used the FL signal of the lipid bilayer in each case.

To apply statistical analysis to the Ca^{2+} influx curves, we calculated the area under de curve (AUC) for each cell in each condition (WT, DGK$\zeta^{-/-}$ and R59-treated) and then compared the obtained AUC values with those of the control condition (untreated WT). To obtain the AUC value per cell, we sectioned the area in three trapezoids and calculated the area of each one; the AUC is the sum of the three trapezoid areas.

Western blot analysis

Freshly isolated primary B cells (5 x 10^6) were cultured on a p48 plate in depletion medium (0.5 ml complete RPMI, 1 h), in the presence of 10 μM R59 when needed, and then stimulated in Ab-coated (goat anti-mouse IgM, μ-specific; Jackson ImmunoResearch) p48 plate for the indicated times. Wells were pre-coated with 5 μg/ml Ab in PBS (1 h, 37ºC), washed and used. For DGK isoforms or phosphorylated PAK1/2 detection, isolated B cells (5 x 10^6) were cultured in complete RPMI 10%FCS, without or with 10 μM R59 or 0.1 mM PA, for 1 h and then collected. Cells were lysed in lysis buffer (10 mM Tris-HCL pH 7.4, 150 mM NaCl, 1 mM EDTA)/1% Triton-X100 with protease and phosphatase inhibitors (Roche; 30 min, 4ºC). Lysates were centrifuged (14,000 rpm, 30 min, 4ºC), supernatants collected and stored at -80ºC. Total protein was quantified with Micro BCA Protein Assay kit (Thermo Scientific), separated by SDS-PAGE and transferred to PVDF membranes (BioRad). Blots were blocked with TBS-T (10 mM Tris-HCl pH 8.0, 150 mM NaCl, 0.1% Tween-20)/5% BSA (1 h, RT), and incubated with rabbit anti-DGKζ (ab105195; Abcam), anti-DGKα (11547-1-AP; Proteintech), anti-phospho (S473)-Akt (Cell Signaling), anti-phospho (Thr18/Ser19)-MLC (Cell Signaling), anti-phospho (S144)-PAK1/(S141)-PAK2 (Cell Signaling) or loading control mouse anti-α-tubulin (clone DM1A; Sigma) or rabbit anti-GAPDH (FL305, Santa Cruz Biotech) (overnight, 4ºC), followed by horseradish peroxidase-conjugated secondary antibodies (DAKO; 1 h, RT). The signal was detected with the enhanced chemiluminescence detection system (ECL; GE Healthcare). Signal intensity values in arbitrary units (AU) for each protein were quantified using FiJi (NIH) software, normalized to tubulin.

Immunization

Freshly isolated CD45.2^{+} WT or DGK$\zeta^{-/-}$ B cells (5-8 x 10^{6}) were adoptively transferred to CD45.1^{+} immunocompetent mice by intravenous injection. 24 h later mice were immunized intraperitoneally with NIP-OVA (200 μg; N-5041-10, Biosearch Technology) complexed with Alum (100 μl; 77161, Thermo Scientific) diluted 1:1 in PBS (0.2 ml final volume). Seven days post-immunization, spleens were harvested and processed for CD45.2^{+} B cell population analysis by flow cytometry.

Flow cytometry

B cells were stained with fluorochrome-conjugated (FITC, PE, or APC) rat anti-mouse IgD, CD19, CD25, CD69, or CD86 (BioLegend), and DyLight-649-conjugated Fab fragment goat anti-mouse IgM, μ-specific (Jackson ImmunoResearch) (30 min, 4ºC). Samples were acquired in a FACSCalibur cytometer (BD Biosciences). Splenocytes obtained from immunization assays were stained with the following fluorochrome-conjugated antibodies mix: rat anti-mouse-CD45.1 (APC-Cy7), -CD45.2 (APC), -B220 (V450), -CD95 (PE-Cy7), -GL7 (FITC) and PE-conjugated NP(36) (N-5070-1, Biosearch Technology) for GC B cell analysis; rat anti-mouse-CD45.1 (APC-Cy7), -CD45.2 (Per-CP5.5), -CD19 (PE-Cy7), -CD138 (APC), -IgG1 (PE), -IgD (V450), and -IgM (biotin) plus FITC-conjugated streptavidin for PC and IgG1^{+} B cell analysis; all antibodies from BD Biosciences. Samples were acquired in a FACSCanto II cytometer. Data was analyzed using FlowJo software (BD Biosciences).

Traction Force Microscopy (TFM)

Polyacrylamide (PAA) gels were produced in 35-mm FD35 fluorodishes (World Precision Instruments, Inc). Dishes were first treated by UV irradiation (2 min), then with 3-aminopropyltrimethoxysilane (APTMS; 5 min), and finally washed thoroughly in

distilled water before PAA gels preparation. Hydrophobic coverslips were prepared by incubation in Sigmacote (3 min; Sigma-Aldrich), followed by thorough washing and drying. A 500 Pa gel was prepared by diluting 40% PAA and 2% bis-acrylamide solutions to obtain stock solutions of 12% PAA/0.1% bis-acrylamide. We sonicated 167 μl of this solution with 1% of 0.2 μm diameter carboxilated fluorescent (660/680) beads (ThermoFisher Scientific), and then added 0.2 μl of TEMED and 1% ammonium persulfate and mixed vigorously, to initiate polymerization. A volume of 9 μl of the PAA mixture was immediately pipetted onto the surface of the Fluorodish and a Sigmacote-activated coverslip was carefully placed on top. Fluorodishes were immediately inverted, to bring the beads to the surface of the gel. Polymerization was completed in 45 min; the top coverslip was then slowly peeled off and the gel immediately immersed in PBS. Sulfo-SANPAH (Sigma-Aldrich), a surface functionalizing reagent with an amine-binding group and a photoactivable azide group, was used to crosslink molecules to the surface of the gel. Sulpho-SANPAH (150 μl of 0.5 mg/ml stock in Hepes 10 mM) was attached to the gel surface through UV light activation (2 min); the gels were then washed with PBS and the process repeated. The gel was washed thoroughly with PBS and coated with 100μl (10 μg/ml) su-Ag (rat anti-κ light chain monoclonal antibody; clone187.1; BD Biosciences) alone or mixed with recombinant mouse ICAM-1-Fc (10 μg/ml; BioLegend) by overnight incubation at 4°C. Freshly isolated WT and DGK$\zeta^{-/-}$ B cells were mixed at 1:1 ratio (1 x 10^6), being one of them labeled with CFSE-tracer to distinguished them, then added to the gels and imaged. Assays were performed in complete RPMI/10% FCS medium. All TFM movies were acquired at 37°C/4.5% CO_2 on an inverted spinning disk confocal microscope (Eclipse Ti Nikon/Roper spinning head) with a 60x/1.4NA oil immersion objective (pixel size 108 nm) with MetaMorph software (Molecular Device,

France) and HQ2 Coolsnap Photometric camera; time lapse was typically at 1 image/5 sec frame rate and lasted for 15 min.

The traction force algorithm was based on that used by Butler and colleagues (*57*) and modified by Mandal and colleagues (*58*). Force reconstruction was conducted with the assumption that the substrate is a linear elastic half space, using Fourier Transform Traction Cytometry with Tikhonov regularization (regularization parameter was set to $5x10^{-19}$). The bead position in reference image and deformed one was measured using Multi Target Tracking (MTT) algorithm Bertaux (*59*). The problem of calculating the stress field from the displacement was solved in Fourier space then inverted back to real space. The final stress field was obtained on a grid with 0.432 μm spacing (4 pixels). All calculations and image processing were performed in Matlab. The mask of the cell (defined by user based on fluorescence or bright field images) increased by 10% (dilation of the binary image using Matlab morphological tools) was used as domain of integration for the energy.

Given the B cell size, the density of beads, and the magnitude of displacement, some parameters needed optimization for the analysis. In particular for the detection algorithm (MTT): search window size (5 pixels), particle radius (2.5 pixels) and maximum distance for nearest neighbor (4 pixels). Same parameters were applied for noise detection by measuring force in a non-stressed area not too far from the cell. Further calculations based on the output of the algorithm were performed to extract the total strain energy (scalar product force by displacement integrated over the entire cell area). Noise higher than a certain threshold (chosen at $3e10^{-17}$J) indicates poorly acquired data (e.g. due to defocus): the corresponding frames were eliminated from the analysis.

Micropipette Force Probe (MFP)

MFP (*21*) uses a flexible glass micropipette as a cantilever to measure pushing/pulling forces generated by a single cell. We added supplementary single-cell rheometer capabilities to measure the mechanical properties of the cell during its activation. Micropipettes were prepared as described previously (*21, 47, 60, 61*) by pulling borosilicate glass capillaries (Harvard Apparatus, Holliston, MA, USA) with a P-97 micropipette puller (Sutter Instruments, Novato, CA, USA), cutting them with an MF-200 microforge (World Precision Instruments, Sarasota, FL, USA) and bending them at a 45° angle with an MF-900 microforge (Narishige, Tokyo, Japan). Micropipettes were held by micropipette holders (IM-H1, Narishige) placed at a 45° angle relative to a horizontal plane, so that their tips were in the focal plane of an inverted microscope under bright-field illumination (TiE, Nikon Instruments, Tokyo, Japan) equipped with a 100× oil immersion, 1.3 NA objective (Nikon Instruments) and placed on an air suspension table (Newport). The flexible micropipette was linked to a non-motorized micropositioner (Thorlabs, Newton, NJ, USA) placed on top of a single-axis stage controlled with a piezo actuator (TPZ001; Thorlabs). The bending stiffness k of the flexible micropipette (about 0.2 nN/μm) was measured against a standard microindenter previously calibrated with a commercial force probe (model 406A; Aurora Scientific, Aurora, ON, Canada). The flexible micropipette aspirates a GPI-ICAM-1-containing lipid-coated bead with tethered su-Ag (100 molec/μm^2) while a second (rigid) micropipette holds a B cell at its tip. The B cell is brought in adequate position using a motorized micromanipulator (MP-285; Sutter Instruments). Experiments were performed in glass-bottom Petri dishes (Fluorodish, WPI, Sarasota, FL, USA) filled with about 5 ml of complete RPMI/10%FCS at RT. Images were acquired using a Flash 4.0 CMOS camera (Hamamatsu Photonics, Hamamatsu City, Japan). In order to perform rheological experiments, the setup automatically detects at a rate of 400-500 Hz the position of the bead at the tip of the

force probe (X_{bead}) and imposes the position of the base of the flexible micropipette by regulating the position of the piezo stage. The deflection of the force probe is the difference between the position of the bead and the position of the piezo stage. The force applied to the cell is the product of this deflection by the bending stiffness *k*. A retroaction implemented in Matlab (Mathworks) regulating both the camera by the Micromanager software (Edelstein 2014) and the piezo stage, moves the latter in reaction to the measurement of the bead position in order to keep a desired deflection of the cantilever. In this way, a controlled force is applied to the cell at any given time. The experiment was decomposed in two phases. During a first phase, the base of the force probe was translated at constant velocity v = 1 μm/s towards the cell, leading to an increasing compressive force until a maximum compressive force of 240 pN was reached. Young's modulus of the cell was obtained by post-processing the recordings made during this phase, as previously described (*60*). Then, the algorithm automatically switched to a second phase during which an oscillatory force F was applied to the cell with an average force F_0=60 pN, an amplitude ΔF = 20 pN and at a frequency *f*=1 Hz. Knowing the position of the bead, we could deduce the changes in cell length (L) over time. L was approximatively sinusoidal with an average value L_0, an amplitude ΔL, and a phase lag φ relative of the imposed force. This phase lag witnesses the fact that the cell is not purely elastic but also viscous. In this study, we focused on the variations of the elastic properties of the cell, that we quantified with the stiffness K' of the cell that is expressed as $K' = (\Delta F/\Delta L)\cos\varphi$ (see Supplemental Methods for K' parameter quantification). The average length L_0 varies as allows this monitoring cell growth or shrinkage.

Statistical analysis

Graphs and statistical analyses were performed using GraphPad Prism 6.0f software. Two-tailed unpaired Student's t-test was applied; * $p<0.05$; ** $p<0.01$; *** $p<0.001$; **** $p<0.0001$.

REFERENCES

1. I. Merida, E. Andrada, S. I. Gharbi, A. Avila-Flores, Redundant and specialized roles for diacylglycerol kinases alpha and zeta in the control of T cell functions. *Sci Signal* **8**, re6 (2015).
2. G. Baldanzi, V. Bettio, V. Malacarne, A. Graziani, Diacylglycerol Kinases: Shaping Diacylglycerol and Phosphatidic Acid Gradients to Control Cell Polarity. *Front Cell Dev Biol* **4**, 140 (2016).
3. M. L. Wheeler, M. B. Dong, R. Brink, X. P. Zhong, A. L. DeFranco, Diacylglycerol kinase zeta limits B cell antigen receptor-dependent activation of ERK signaling to inhibit early antibody responses. *Sci Signal* **6**, ra91 (2013).
4. J. Saez de Guinoa, L. Barrio, Y. R. Carrasco, Vinculin arrests motile B cells by stabilizing integrin clustering at the immune synapse. *J Immunol* **191**, 2742-2751 (2013).
5. Y. R. Carrasco, S. J. Fleire, T. Cameron, M. L. Dustin, F. D. Batista, LFA-1/ICAM-1 interaction lowers the threshold of B cell activation by facilitating B cell adhesion and synapse formation. *Immunity* **20**, 589-599 (2004).
6. A. Grakoui *et al.*, The immunological synapse: a molecular machine controlling T cell activation. *Science* **285**, 221-227 (1999).
7. C. R. Monks, B. A. Freiberg, H. Kupfer, N. Sciaky, A. Kupfer, Three-dimensional segregation of supramolecular activation clusters in T cells. *Nature* **395**, 82-86 (1998).
8. M. Spitaler, E. Emslie, C. D. Wood, D. Cantrell, Diacylglycerol and protein kinase D localization during T lymphocyte activation. *Immunity* **24**, 535-546 (2006).
9. S. I. Gharbi *et al.*, Diacylglycerol kinase zeta controls diacylglycerol metabolism at the immunological synapse. *Mol Biol Cell* **22**, 4406-4414 (2011).
10. R. P. Joshi *et al.*, The zeta isoform of diacylglycerol kinase plays a predominant role in regulatory T cell development and TCR-mediated ras signaling. *Sci Signal* **6**, ra102 (2013).
11. F. Chianale *et al.*, Diacylglycerol kinase alpha mediates HGF-induced Rac activation and membrane ruffling by regulating atypical PKC and RhoGDI. *Proc Natl Acad Sci U S A* **107**, 4182-4187 (2010).
12. Y. Yakubchyk *et al.*, Regulation of neurite outgrowth in N1E-115 cells through PDZ-mediated recruitment of diacylglycerol kinase zeta. *Mol Cell Biol* **25**, 7289-7302 (2005).
13. H. Abramovici, A. B. Hogan, C. Obagi, M. K. Topham, S. H. Gee, Diacylglycerol kinase-zeta localization in skeletal muscle is regulated by phosphorylation and interaction with syntrophins. *Mol Biol Cell* **14**, 4499-4511 (2003).
14. E. Rainero *et al.*, Diacylglycerol kinase alpha controls RCP-dependent integrin trafficking to promote invasive migration. *J Cell Biol* **196**, 277-295 (2012).
15. G. H. Jenkins, P. L. Fisette, R. A. Anderson, Type I phosphatidylinositol 4-phosphate 5-kinase isoforms are specifically stimulated by phosphatidic acid. *J Biol Chem* **269**, 11547-11554 (1994).
16. A. N. Roach *et al.*, Phosphatidic acid regulation of PIPKI is critical for actin cytoskeletal reorganization. *J Lipid Res* **53**, 2598-2609 (2012).
17. G. Di Paolo, P. De Camilli, Phosphoinositides in cell regulation and membrane dynamics. *Nature* **443**, 651-657 (2006).

18. E. Andrada *et al.*, Diacylglycerol kinase zeta limits the polarized recruitment of diacylglycerol-enriched organelles to the immune synapse in T cells. *Sci Signal* **9**, ra127 (2016).
19. A. Chauveau, A. Le Floc'h, N. S. Bantilan, G. A. Koretzky, M. Huse, Diacylglycerol kinase alpha establishes T cell polarity by shaping diacylglycerol accumulation at the immunological synapse. *Sci Signal* **7**, ra82 (2014).
20. R. Basu, M. Huse, Mechanical Communication at the Immunological Synapse. *Trends Cell Biol* **27**, 241-254 (2017).
21. A. Sawicka *et al.*, Micropipette force probe to quantify single-cell force generation: application to T-cell activation. *Mol Biol Cell* **28**, 3229-3239 (2017).
22. E. Natkanski *et al.*, B cells use mechanical energy to discriminate antigen affinities. *Science* **340**, 1587-1590 (2013).
23. A. Le Floc'h *et al.*, Annular PIP3 accumulation controls actin architecture and modulates cytotoxicity at the immunological synapse. *J Exp Med* **210**, 2721-2737 (2013).
24. H. Abramovici *et al.*, Diacylglycerol kinase zeta regulates actin cytoskeleton reorganization through dissociation of Rac1 from RhoGDI. *Mol Biol Cell* **20**, 2049-2059 (2009).
25. J. Wang *et al.*, Profiling the origin, dynamics, and function of traction force in B cell activation. *Sci Signal* **11**, (2018).
26. T. Numaga *et al.*, Ca2+ influx and protein scaffolding via TRPC3 sustain PKCbeta and ERK activation in B cells. *J Cell Sci* **123**, 927-938 (2010).
27. M. I. Yuseff, A. M. Lennon-Dumenil, B Cells use Conserved Polarity Cues to Regulate Their Antigen Processing and Presentation Functions. *Front Immunol* **6**, 251 (2015).
28. C. R. Nowosad, K. M. Spillane, P. Tolar, Germinal center B cells recognize antigen through a specialized immune synapse architecture. *Nat Immunol* **17**, 870-877 (2016).
29. M. I. Yuseff *et al.*, Polarized secretion of lysosomes at the B cell synapse couples antigen extraction to processing and presentation. *Immunity* **35**, 361-374 (2011).
30. R. Ard *et al.*, Diacylglycerol kinase zeta regulates RhoA activation via a kinase-independent scaffolding mechanism. *Mol Biol Cell* **23**, 4008-4019 (2012).
31. V. D. Delorme-Walker *et al.*, Pak1 regulates focal adhesion strength, myosin IIA distribution, and actin dynamics to optimize cell migration. *J Cell Biol* **193**, 1289-1303 (2011).
32. S. Dharmawardhane, L. C. Sanders, S. S. Martin, R. H. Daniels, G. M. Bokoch, Localization of p21-activated kinase 1 (PAK1) to pinocytic vesicles and cortical actin structures in stimulated cells. *J Cell Biol* **138**, 1265-1278 (1997).
33. A. Nishikimi *et al.*, Sequential regulation of DOCK2 dynamics by two phospholipids during neutrophil chemotaxis. *Science* **324**, 384-387 (2009).
34. Y. Mori *et al.*, Transient receptor potential 1 regulates capacitative Ca(2+) entry and Ca(2+) release from endoplasmic reticulum in B lymphocytes. *J Exp Med* **195**, 673-681 (2002).
35. P. Lucas, K. Ukhanov, T. Leinders-Zufall, F. Zufall, A diacylglycerol-gated cation channel in vomeronasal neuron dendrites is impaired in TRPC2 mutant mice: mechanism of pheromone transduction. *Neuron* **40**, 551-561 (2003).
36. T. Hofmann *et al.*, Direct activation of human TRPC6 and TRPC3 channels by diacylglycerol. *Nature* **397**, 259-263 (1999).
37. T. Okada *et al.*, Molecular and functional characterization of a novel mouse transient receptor potential protein homologue TRP7. Ca(2+)-permeable cation

channel that is constitutively activated and enhanced by stimulation of G protein-coupled receptor. *J Biol Chem* **274**, 27359-27370 (1999).
38. M. Nishida *et al.*, Amplification of receptor signalling by Ca2+ entry-mediated translocation and activation of PLCgamma2 in B lymphocytes. *EMBO J* **22**, 4677-4688 (2003).
39. A. Reversat *et al.*, Polarity protein Par3 controls B-cell receptor dynamics and antigen extraction at the immune synapse. *Mol Biol Cell* **26**, 1273-1285 (2015).
40. E. J. Quann, E. Merino, T. Furuta, M. Huse, Localized diacylglycerol drives the polarization of the microtubule-organizing center in T cells. *Nat Immunol* **10**, 627-635 (2009).
41. E. J. Quann, X. Liu, G. Altan-Bonnet, M. Huse, A cascade of protein kinase C isozymes promotes cytoskeletal polarization in T cells. *Nat Immunol* **12**, 647-654 (2011).
42. D. Obino *et al.*, Actin nucleation at the centrosome controls lymphocyte polarity. *Nat Commun* **7**, 10969 (2016).
43. M. Huse, Mechanical forces in the immune system. *Nat Rev Immunol* **17**, 679-690 (2017).
44. W. A. Comrie, A. Babich, J. K. Burkhardt, F-actin flow drives affinity maturation and spatial organization of LFA-1 at the immunological synapse. *J Cell Biol* **208**, 475-491 (2015).
45. K. Ling, N. J. Schill, M. P. Wagoner, Y. Sun, R. A. Anderson, Movin' on up: the role of PtdIns(4,5)P(2) in cell migration. *Trends Cell Biol* **16**, 276-284 (2006).
46. J. Husson, K. Chemin, A. Bohineust, C. Hivroz, N. Henry, Force generation upon T cell receptor engagement. *PLoS One* **6**, e19680 (2011).
47. R. Basu *et al.*, Cytotoxic T Cells Use Mechanical Force to Potentiate Target Cell Killing. *Cell* **165**, 100-110 (2016).
48. R. K. Abbott *et al.*, Precursor Frequency and Affinity Determine B Cell Competitive Fitness in Germinal Centers, Tested with Germline-Targeting HIV Vaccine Immunogens. *Immunity* **48**, 133-146 e136 (2018).
49. P. U. Prinz *et al.*, High DGK-alpha and disabled MAPK pathways cause dysfunction of human tumor-infiltrating CD8+ T cells that is reversible by pharmacologic intervention. *J Immunol* **188**, 5990-6000 (2012).
50. E. K. Moon *et al.*, Multifactorial T-cell hypofunction that is reversible can limit the efficacy of chimeric antigen receptor-transduced human T cells in solid tumors. *Clin Cancer Res* **20**, 4262-4273 (2014).
51. X. P. Zhong *et al.*, Enhanced T cell responses due to diacylglycerol kinase zeta deficiency. *Nat Immunol* **4**, 882-890 (2003).
52. B. A. Olenchock *et al.*, Disruption of diacylglycerol metabolism impairs the induction of T cell anergy. *Nat Immunol* **7**, 1174-1181 (2006).
53. K. Okkenhaug *et al.*, Impaired B and T cell antigen receptor signaling in p110delta PI 3-kinase mutant mice. *Science* **297**, 1031-1034 (2002).
54. Y. Kunisaki *et al.*, DOCK2 is a Rac activator that regulates motility and polarity during neutrophil chemotaxis. *J Cell Biol* **174**, 647-652 (2006).
55. M. J. Barnden, J. Allison, W. R. Heath, F. R. Carbone, Defective TCR expression in transgenic mice constructed using cDNA-based alpha- and beta-chain genes under the control of heterologous regulatory elements. *Immunol Cell Biol* **76**, 34-40 (1998).
56. J. Saez de Guinoa, L. Barrio, M. Mellado, Y. R. Carrasco, CXCL13/CXCR5 signaling enhances B-cell receptor-triggered B-cell activation by shaping cell dynamics. *Blood* **118**, 1560-1569 (2011).

57. J. P. Butler, I. M. Tolic-Norrelykke, B. Fabry, J. J. Fredberg, Traction fields, moments, and strain energy that cells exert on their surroundings. *Am J Physiol Cell Physiol* **282**, C595-605 (2002).
58. K. Mandal, I. Wang, E. Vitiello, L. A. Orellana, M. Balland, Cell dipole behaviour revealed by ECM sub-cellular geometry. *Nat Commun* **5**, 5749 (2014).
59. A. Serge, N. Bertaux, H. Rigneault, D. Marguet, Dynamic multiple-target tracing to probe spatiotemporal cartography of cell membranes. *Nat Methods* **5**, 687-694 (2008).
60. L. Guillou, A. Babataheri, P. H. Puech, A. I. Barakat, J. Husson, Dynamic monitoring of cell mechanical properties using profile microindentation. *Sci Rep* **6**, 21529 (2016).
61. L. Guillou *et al.*, T-lymphocyte passive deformation is controlled by unfolding of membrane surface reservoirs. *Mol Biol Cell* **27**, 3574-3582 (2016).

Acknowledgements: The authors thank Mario Mellado and C. Rodrigo Jimenez-Saiz (CNB-CSIC) for critical review of the manuscript, and Martial Balland (Liphy, Grenoble) for providing tools and suggestions for TFM experiments. The authors acknowledge the PICT-IBiSA imaging platform at Institut Curie, member of the French National Research Infrastructure France-BioImaging (ANR-10-INBS-04). **Funding:** SVMC is supported by an FPI contract from the Spanish Ministry of Economy (MINECO; BES-2014-068006). This work was supported by grants from the MINECO (BFU2013-48828-P) and from the Worldwide Cancer Research (WCR; grant reference number 15-1322). JH has benefited from the financial support of the LabeX LaSIPS (ANR-10-LABX-0040-LaSIPS) managed by the French National Research Agency under the "Investissements d'avenir" program (nº ANR-11-IDEX-0003-02), and from a PEPS CNRS funding. **Author contributions:** SVM-C designed parts of the study, performed experiments, analyzed the data and assisted in manuscript preparation; SG and SR-G performed some experiments, analyzed data and assisted in manuscript preparation; AM-R and BA performed in vitro antigen presentation and in vivo immunization experiments, assisted in data analysis and provided input into the project; RL and IM provided DGK$\zeta^{-/-}$ and DGK$\alpha^{-/-}$ mice, DGKζ constructs and input into the project; JP, AML-D and PP performed and analyzed TFM experiments, and provided input into the project; JH performed and analyzed MFP experiments, and provided input into the project; YRC designed and supervised all aspects of the work and wrote the manuscript. **Competing interests:** The authors declare that they have no competing interests. **Data and materials availability:** All data needed to evaluate the conclusions in the paper are present in the paper or the Supplementary Material.

FIGURE LEGENDS

Figure 1. DGKζ dysfunction alters LFA-1 adhesion and F-actin content at the B cell synapse. B cells settled on ICAM-1/CXCL13 planar lipid bilayers loaded with su-Ag (20 molec/μm^2) for 10 min, and were imaged or fixed for immunofluorescence. (A) DIC, IRM and fluorescence su-Ag images at the contact plane of representative IS-forming WT, DGKζ$^{-/-}$ and R59-treated B cells. (B) Frequencies of IS formation. (C, D) Values of contact area (left), su-Ag central cluster area (cSMAC; mid-panel) and total su-Ag fluorescence (FL) (in arbitrary FL units, AU; right) for (C) DGKζ$^{-/-}$ and (D) R59-treated B cells with established IS compared to WT. Each dot in B represents a single image field, and in C, D a single cell. (E) DIC and FL images of F-actin (white) for representative IS-forming WT, DGKζ$^{-/-}$ and R59-treated B cells, fixed at 10 min. (F) Values of total F-actin FL at the IS in each case and in presence of distinct su-Ag densities (20 and 5 molec/μm^2). (G) As in E but of vinculin (green) and su-Ag (red). (H) As in F but for total vinculin FL at the IS. Each dot in F and H is a single cell. Data in B and H are the merge of two experiments (n = 4); data for a representative experiment are shown in C, D (n = 3), and F (n = 4). Scale bar, 2.5 μm. *, p<0.05; **, p<0.01; ****, p<0.0001 by two-tailed unpaired Student's t-test.

Figure 2. PA generation promotes LFA-1 adhesion and F-actin polymerization. (A-D) B cells were in contact with ICAM-1/CXCL13 planar lipid bilayers loaded with su-Ag (20 molec/μm^2) for 10 min to establish the IS, imaged, then exposed to 0.1 mM PA (30 min) and imaged or fixed for immunofluorescence. (A) DIC and IRM images for representative WT and DGKζ$^{-/-}$ B cells, untreated or R59-treated, before (none) and after PA exposure. (B) Values of contact area for B cells as in A. (C) DIC and FL images of F-actin for representative B cells as in A, fixed before (none) or after PA exposure. (D)

Values of total F-actin FL at the IS in each condition and for each cell type. (E) DIC and FL images of F-actin for representative WT and DGKζ$^{-/-}$ B cells, untreated or treated with LY294002, fixed at 10 min after contact with planar bilayer as in A. Values of total F-actin FL at the IS in each condition, right. (F) As in E, but for WT and PI3Kδ KD B cells, untreated or R59-treated. (G) DIC and FL images of DOCK2-GFP for representative IS-forming DOCK2-GFP knock-in B cells, untreated or R59-treated, after 10 min in contact with su-Ag-loaded (20 molec/μm^2) planar bilayer. Values of total DOCK2-GFP FL at the IS in each condition, right. (H) Immunoblot of non-treated and R59-treated (1 h) WT and DGKζ$^{-/-}$ B cells, and of transfected A20 B cells sorted for non-expressing (GFP^{neg}; none) or GFP-DGKζ-WT expressing (DGKζ-WT), probed with specified antibodies. For primary B cells, lysates from three mice of each genotype are shown. Quantification of phosphorylated-PAK1 (p-PAK1) and p-PAK2 intensity normalized to loading control (α-Tubulin, α-Tub), bottom. For B-G, each dot is a single cell. Data in B, D, are the merge of two experiments (n = 4); data for a representative experiment are shown in E, F (n = 3), and G (n = 2); data in H are the mean ±SD of three mice and of three A20 transfection experiments. Scale bar, 2.5 μm. *, p<0.05; **, p<0.01; ***, p<0.001; ****, p<0.0001 by two-tailed unpaired Student's t-test.

Figure 3. Mechanical force generation at the B cell synapse is regulated by DGKζ. (A) B cells were allowed to settle on the PAA gels coated with su-Ag or su-Ag plus ICAM-1-Fc, and monitored for up to 15 min. Time-lapse color maps of Stress (in Pascal, Pa) for representative WT and DGKζ$^{-/-}$ B cells on PAA gels in the specified conditions. (B) Left, average values of synaptic traction forces (in Joules) over time for WT and DGKζ$^{-/-}$ B cells in each condition. Each solid line corresponds to the mean of 25-30 measured cells; dotted lines, ±SD (confidence interval). Right, average value of synaptic

traction forces per cell over time; each dot is a cell. Data are pooled of 3 experiments (*n* = 3). (C-J) B cells were monitored while contacting silica beads coated with ICAM-1-containing lipid bilayers unloaded (none) or su-Ag loaded (100 molec/μm^2) by MFP technique. (C) Bright field microscopy images (processed using a high-pass filter for better visualization using the ImageJ software) for representative WT and DGK$\zeta^{-/-}$ B cells activated by a su-Ag-loaded bead. In both examples, the cells are submitted to an oscillary force of 50 pN average, 25 pN amplitude, and 1 Hz frequency. It possible to see that the DGK$\zeta^{-/-}$ B cell in this example generated a shorter protrusion than the WT. (D) Time trace of the su-Ag-loaded bead position (X_{bead}, in μm) for WT and DGK$\zeta^{-/-}$ B cells; each line corresponds to the average value of 10 cells. Data from a representative experiment are shown (*n* = 3). (E) Values of pushing speed (in μm/sec) per cell when contact the su-Ag-loaded bead; each dot is a cell. Data are from two experiments (*n* = 3). (F-G) Mechanical changes during activation. (F) Values of Young's modulus (in Pascal, Pa) per cell when contacting beads in the indicated conditions (None, in absence of tethered su-Ag); each dot is a cell. Data are the merge of three experiments (*n* = 3). (G) Left, Time evolution of cell stiffness K' (in nanoNewton (nN)/μm) averaged over cells; each line corresponds to the average value of 20 cells. Data are the merge of two experiments (*n* = 3). Right, Cell stiffness K' averaged over 250 sec following contact with a bead; each dot is a cell. Data are the merge of 3 experiments (*n* = 3). (H) Bright field microscopy images (processed as above) for representative untreated and R59-treated WT B cells activated by a su-Ag-loaded bead, as in C. (I) Values of Young's modulus as in F but for untreated and R59-treated (R59) WT B cells. (J) As in G, but for untreated and R59-treated (R59) WT B cells. Data in I, J are pooled of 3 experiments (*n* = 3). Scale bar, 5 μm. *, $p<0.05$; **, $p<0.01$; ****, $p<0.0001$ by two-tailed unpaired Student's *t*-test.

Figure 4. DGKζ regulates BCR-triggered B cell activation in the context of the IS. (A) Fluo4FF-labeled WT, DGK$\zeta^{-/-}$ and R59-treated B cells were monitored for Ca^{2+} influx at early times of IS formation on ICAM-1/CXCL13 planar lipid bilayers loaded with su-Ag (20 molec/μm^2). Fluorescence Fluo4FF images of representative B cells over time are shown. (B) Left, values of total Fluo4FF FL (in AU) over time; data shown as the mean ± SD of 30 B cells/condition. Right, to statistically compared the Fluo4FF FL data, we calculated the area under the curve (AUC) values per B cell and per condition; each dot represents a cell. (C) WT and DGK$\zeta^{-/-}$ B cells, untreated (none) or R59-treated, were in contact with su-Ag loaded (20 molec/μm^2) ICAM-1/CXCL13 planar lipid bilayers for 10 min and then fixed for immunofluorescence. DIC and FL images of phosphorylated ERK1/2 (p-ERK; green) for representative IS-forming B cells. (D) Values of total p-ERK FL at the IS in each case; each dot is a cell. (E-F) B cells were cultured on ICAM-1/CXCL13 planar lipid bilayers, unloaded (none) or su-Ag-loaded (20 molec/μm^2; su-Ag (20)), for 20 h and then collected for flow cytometry analysis. (E) Representative profiles of CD69, CD25 and CD86 for each case. (F) Frequencies of B cells expressing CD69, CD25 or CD86 (left) and mean fluorescence intensity (MFI) values for these markers (right) in each condition and for each B cell type. (G-H) CFSE-tracer-labeled WT and DGK$\zeta^{-/-}$ B cells, untreated or R59-treated, were co-cultured with pseudo-APC (silica beads coated with ICAM-1/CXCL13 lipid bilayers), unloaded (none) or su-Ag-loaded (1000 molec/μm^2, su-Ag (1000)), at ratio 1:1 and 1:5, in presence of IL-4, for 72 h. (G) Representative profiles of CFSE-tracer in each case. (H) Frequencies of dividing B cells (with diluted CFSE-tracer level) in each condition and for each B cell type. Data from a representative experiment are shown in D (n = 2); each dot represents a cell. Data are pooled of 2 experiments in B (n = 2), in F (n = 4) and of 6 experiments in

H (n = 6). Scale bar, 2.5 μm. *, p<0.05; **, p<0.01; ****, p<0.0001 by two-tailed unpaired Student's t-test.

Figure 5. MTOC translocation, myosin activation and antigen presentation ability are altered in DGKζ$^{-/-}$ and R59-treated B cells. (A) B cells were mixed with unloaded (none) or su-Ag-loaded (20 molec/μm^2; su-Ag (20)) pseudo-APC at 1:1 ratio, cultured for 30 min on poly-L-lysine-coated coverslips and then fixed for immunofluorescence. DIC and FL γ-tubulin (γ-tub; green) images are shown for representative B cell/pseudo-APC conjugates for each indicated condition. Dashed circle, pseudo-APC; scale bar, 2.5 μm. (B) Frequency of B cells as in A, in the specified polarity index (PI) groups. The PI per B cell was estimated as the ratio of "a" and "b" distances (explicative diagram, left); data shown as mean ± SD of 40 B cells in each case. (C) Immunoblot of WT, DGKζ$^{-/-}$ and R59-treated B cells stimulated on Ab-coated plates for the indicated time points, probed with specified antibodies. Quantification of phosphorylated-MLC (p-MLC) intensity normalized to loading control (α-Tubulin, α-Tub), right. (D-E) WT, DGKζ$^{-/-}$ and R59-treated B cells were cultured in contact with ICAM-1/CXCL13 planar lipid bilayers, coated with Alexa Fluor 647-streptavidin (strep) and unloaded (none) or su-Ag/OVA loaded (su-Ag/OVA; 2500 molec/μm^2), for 2 h. Then B cells were collected, treated with trypsin (5 min), and analyzed by flow cytometry for strep fluorescence as readout of su-Ag/OVA extraction. (D) Representative profiles of strep for each case. (E) Frequencies of strep$^+$ B cells (left) and mean fluorescence intensity (MFI) strep values (right) in presence of su-Ag/OVA for each B cell type. Data are pooled of 3 experiments (n = 4 WT and 4 DGKζ$^{-/-}$ mice). (F-I) As in D but, after 2 h incubation with the planar bilayers, B cells were collected, washed, and co-cultured with CFSE-tracer-labeled OTII CD4$^+$ T cells at ratio 1:1 for 72 h. Then, supernatants were collected for IL-2 detection,

and cells were analyzed by flow cytometry. (F) Representative CD25/CD4 dot plots for $CD4^+$ gated OTII T cells in each case and for each condition (B cells exposed to unloaded planar bilayers, none; B cells exposed to su-Ag/OVA-loaded bilayers, su-Ag/OVA); (right) representative profiles of CFSE-tracer for $CD4^+$ $CD25^+$ T cells in each case and for each condition. (G) Frequencies of $CD4^+$ $CD25^+$ T cells and (H) of dividing $CD25^+$ T cells in each case. (I) Values of T cell-mediated IL-2 production at the supernatants of the distinct co-culture conditions. Data in G-I are mean ±SD of 3 experiments (n = 3 WT and 3 DGK$\zeta^{-/-}$ mice). *, p<0.05; **, p<0.01; ***, p<0.001; ****, p<0.0001 by two-tailed unpaired Student's t-test.

Figure 6. Decreased in vivo GC response for DGK$\zeta^{-/-}$ B cells. (A) Experimental design for studying the in vivo response of DGK$\zeta^{-/-}$ compared to WT $CD45.2^+$ B cells in immunocompetent $CD45.1^+$ mice. Gating strategies to analyze $CD45.2^+$ B cells ($CD45.2^+$ $CD19^+$ or $CD45.2^+$ $B220^+$) in spleen are shown on the right. (B) Representative strategy to measure by flow cytometry the frequencies of total GC ($GL7^+$ Fas^+) and NP-specific GC ($GL7^+$ Fas^+ IgD^{neg} NP^+) $CD45.2^+$ $B220^+$ B cells generated 7 days post-immunization with the T cell-dependent antigen Nip-OVA plus Alum; representative density plots for WT and DGK$\zeta^{-/-}$ B cells are shown. Frequencies of gated cells are indicated. (C) Frequencies of total GC B cells (left) and of NP-specific GC B cells (right) in the $CD45.2^+$ $B220^+$ WT or DGK$\zeta^{-/-}$ B cell population at the spleen; each dot represents a mouse. (D) Representative density plots of PC ($CD19^+$ $CD138^+$) and class-switched IgG1 B cell ($CD19^+$ $IgG1^+$) generation for adoptively transferred $CD45.2^+$ WT or DGK$\zeta^{-/-}$ B cells; frequencies of gated cells are indicated. (E) Frequencies of PC and $IgG1^+$ B cells in the $CD45.2^+$ $CD19^+$ WT or DGK$\zeta^{-/-}$ B cell population at the spleen; each dot represents a mouse. (F) Representative density plots of IgM/IgG1 expression on PCs (gated as $CD19^+$

CD138^{+}; PC) for transferred CD45.2^{+} WT or DGK$\zeta^{-/-}$ B cells; frequencies of gated cells are indicated. (G) Frequencies of IgG1^{+} PC (left) and IgM^{+} PC for each case. (H) Representative profile of IgG1 expression on CD19^{+} CD138^{-} B cells (memory-like cells, MC) for transferred CD45.2^{+} WT or DGK$\zeta^{-/-}$ B cells; frequencies of gated cells are indicated. (I) Frequencies of CD138^{-} IgG1^{+} MC for each case. G and I, each dot represents a mouse. Data in C, E, G and I are pooled of 2 independent experiments ($n = 2$). *, $p<0.05$; **, $p<0.01$; ***, $p<0.001$ by two-tailed unpaired Student's *t*-test.

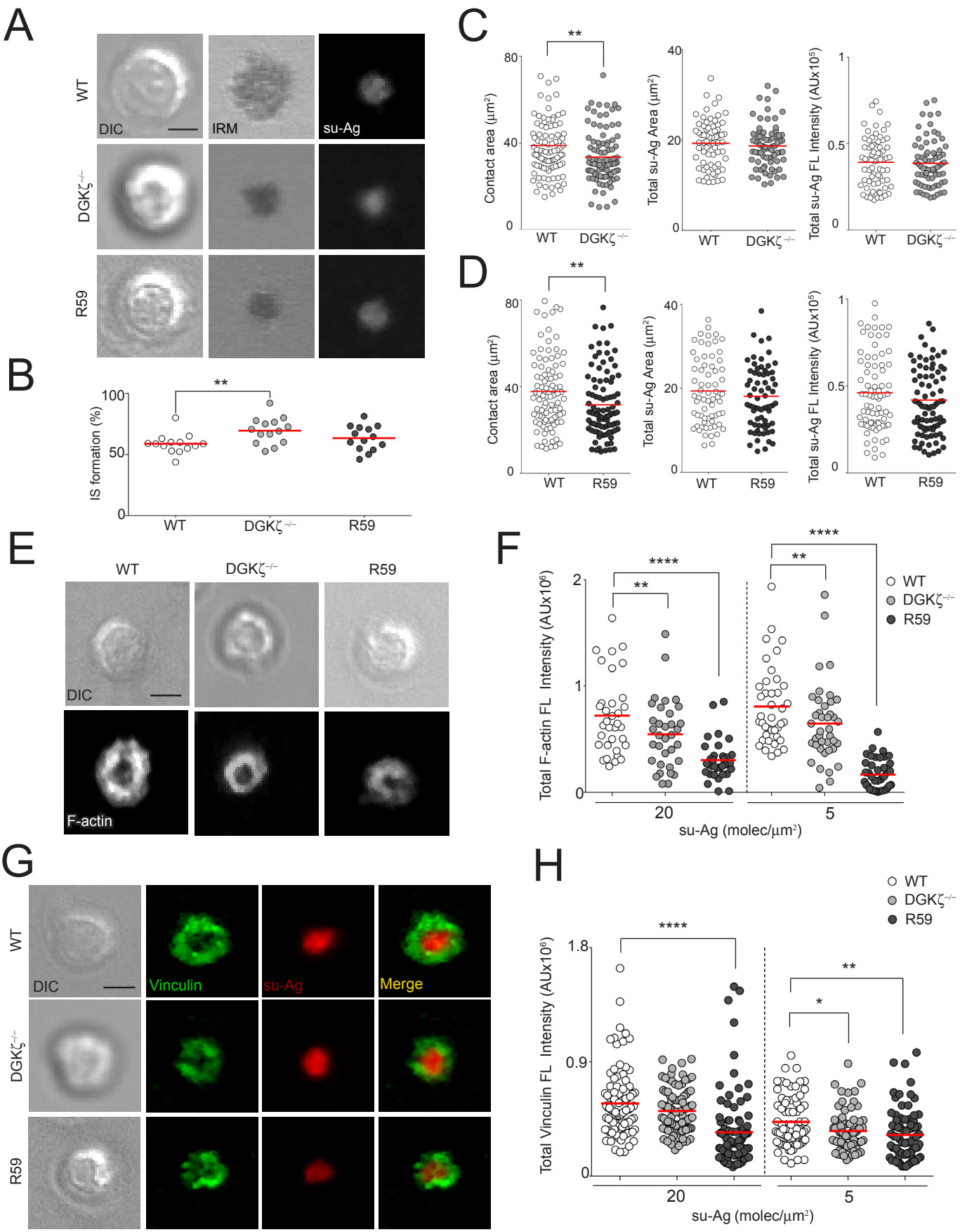

Figure 1. Merino-Cortés *et al.*

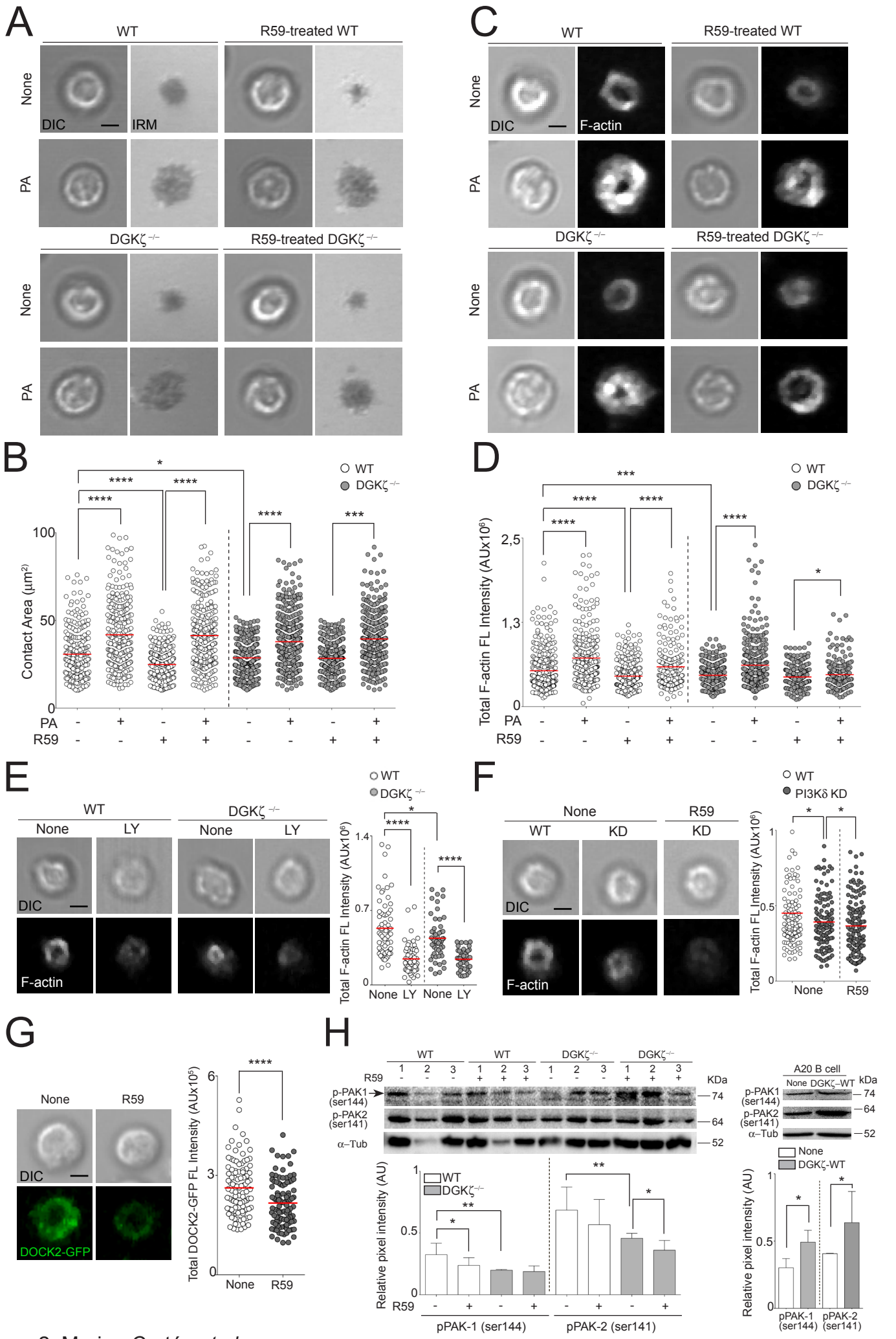

Figure 2. Merino-Cortés *et al.*

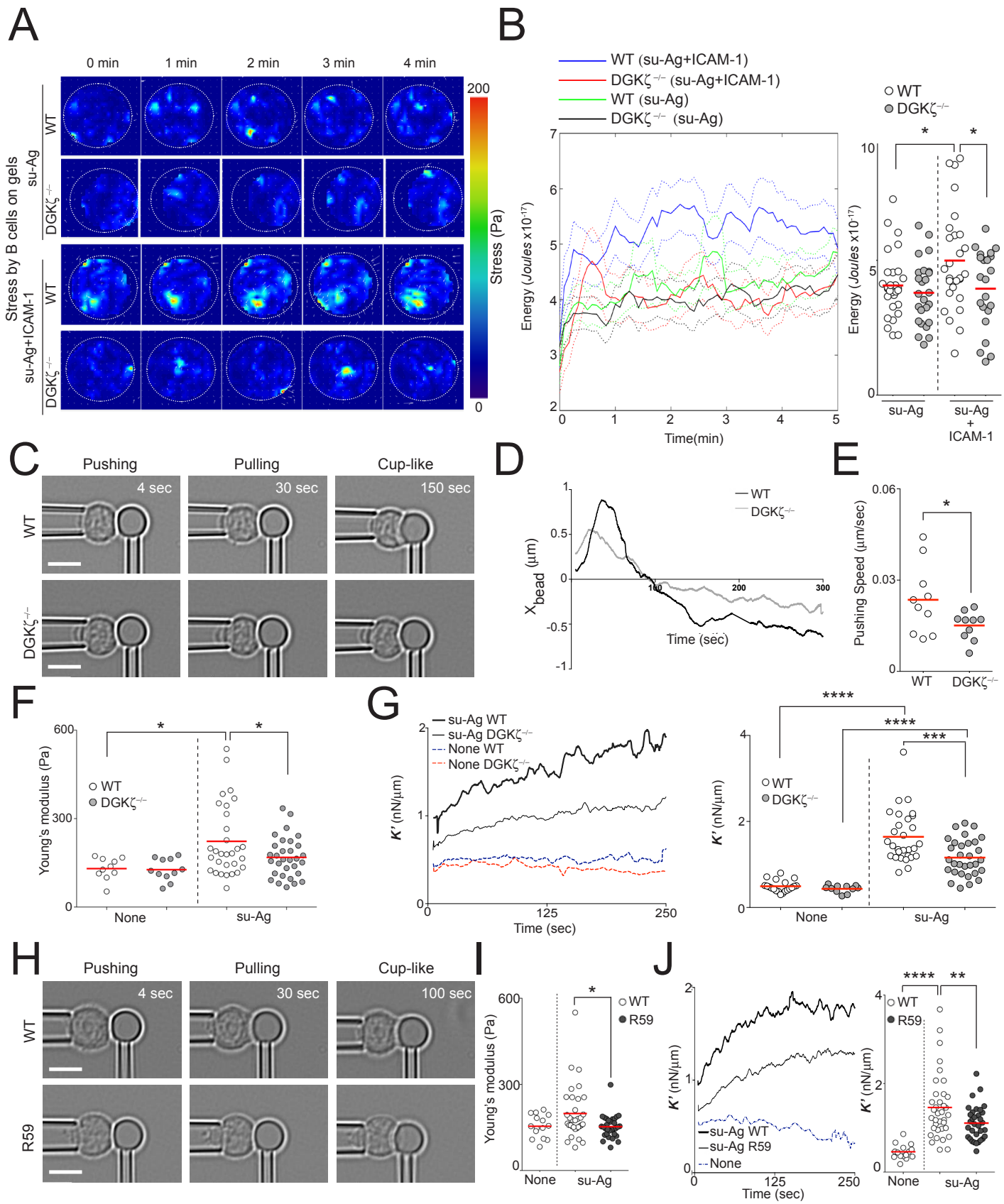

Figure 3. Merino-Cortés *et al.*

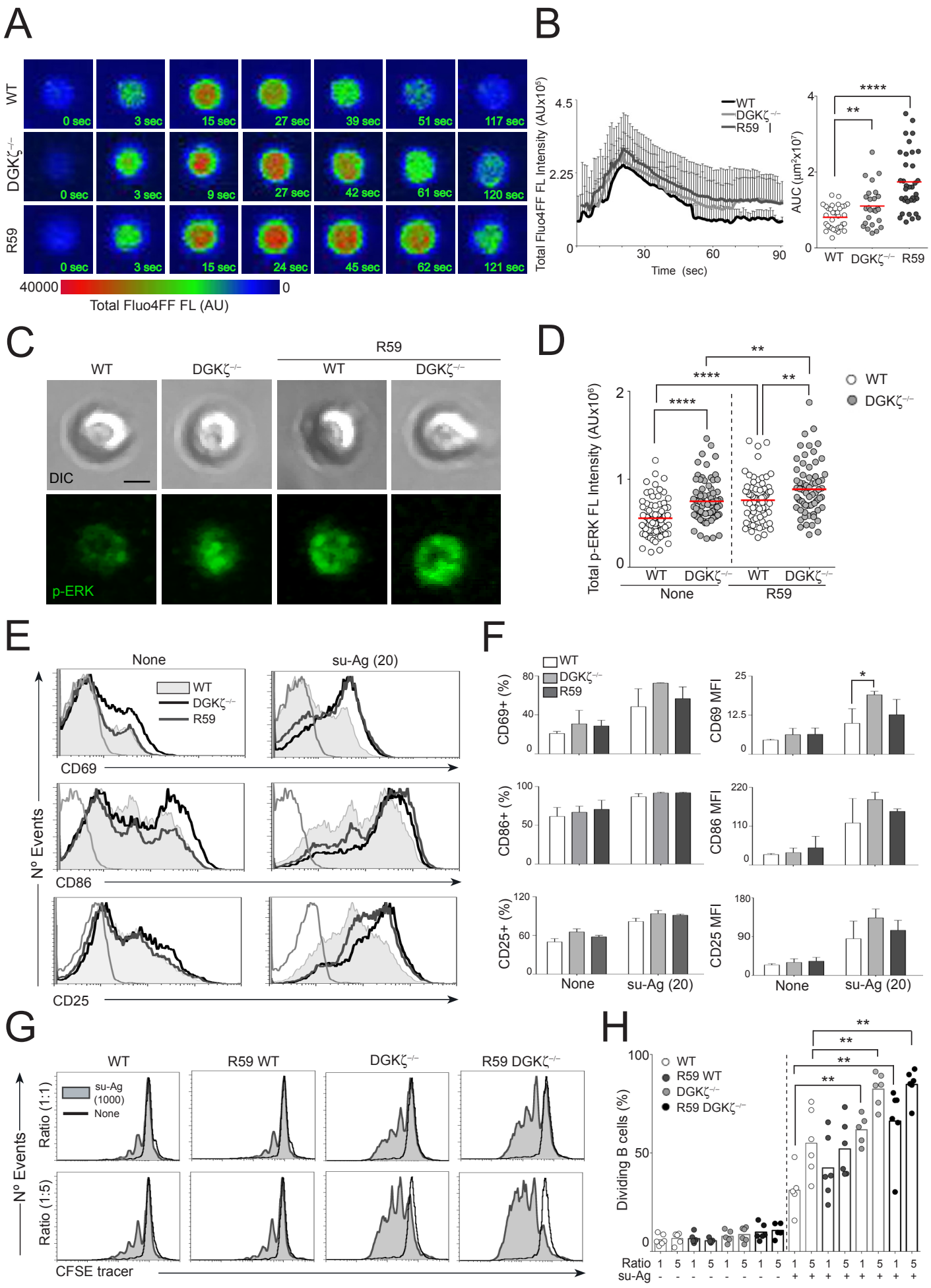

Figure 4. Merino-Cortés *et al.*

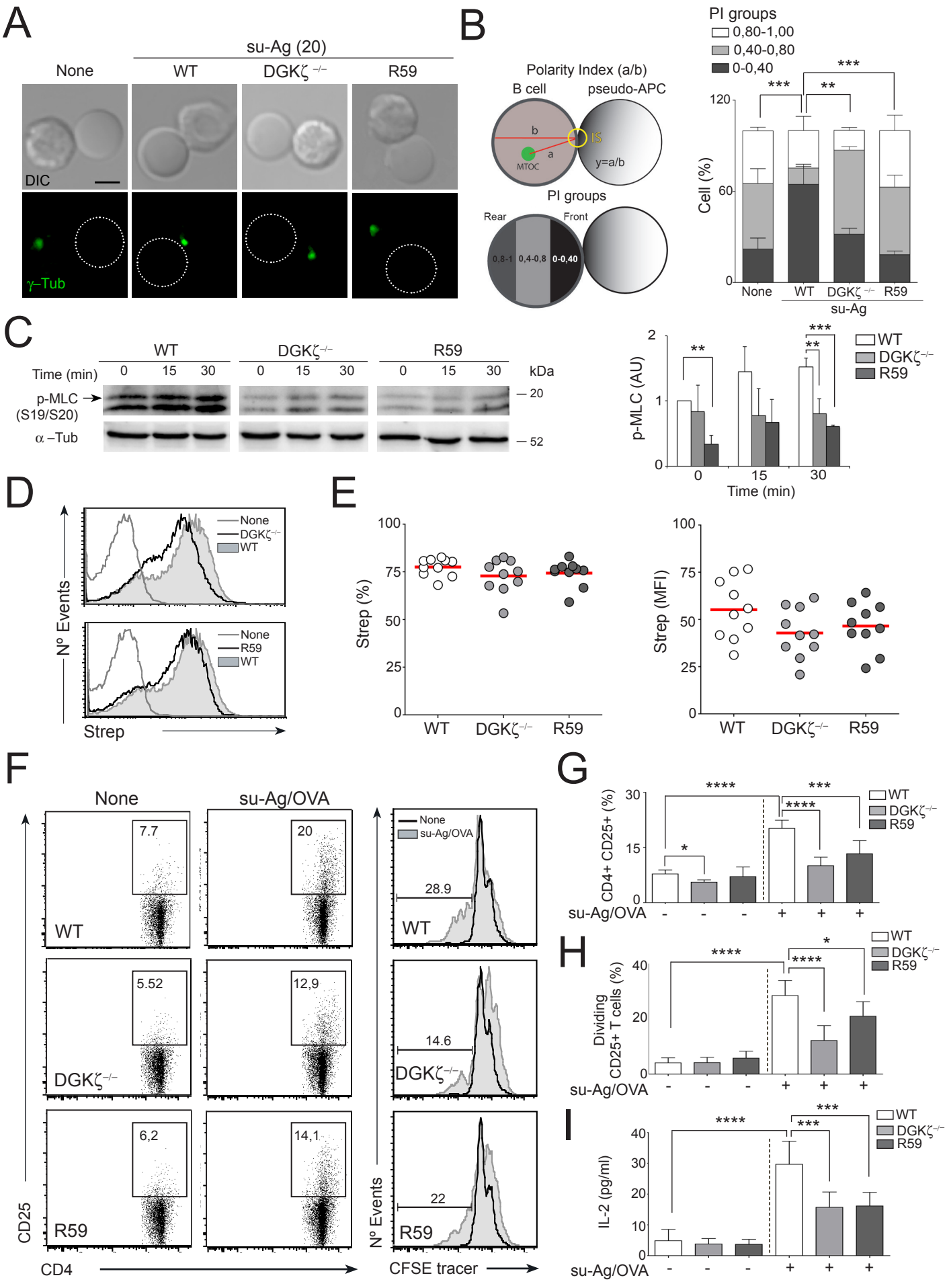

Figure 5. Merino-Cortés *et al.*

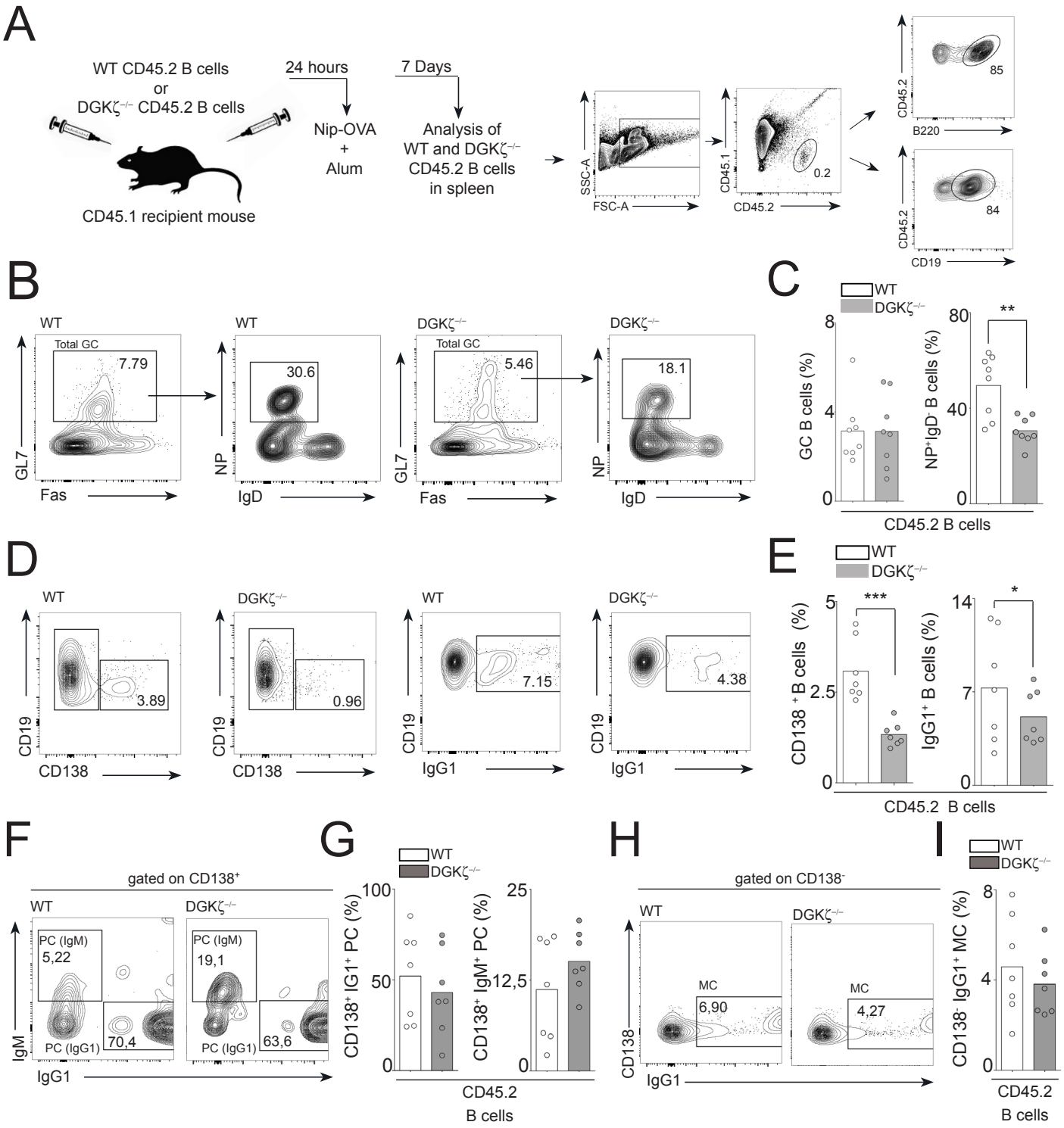

Figure 6. Merino-Cortés *et al.*

SUPPLEMENTARY MATERIAL

SUPPLEMENTARY FIGURE LEGENDS

Figure S1. Characterization of WT, DGKζ$^{-/-}$ and DGKα$^{-/-}$ B cells; DGKζ regulates LFA-1 adhesion at the B cell IS. (A) Immunoblot of untreated and R59-treated (1h) WT and DGKζ$^{-/-}$ B cells, probed with specified antibodies; lysates from three mice of each genotype are shown. Bottom, quantification of DGKζ and DGKα intensity normalized to loading control (α-Tubulin, α-Tub); each dot is a mouse. (B) Representative density plots of IgM/IgD surface expression for WT, DGKζ$^{-/-}$ and DGKα$^{-/-}$ B cells (CD19^{+} gated). (C) Mean fluorescence intensity (MFI) values for IgM (left) and IgD (right) for each B cell type (n = 22 WT, 22 DGKζ$^{-/-}$, and 10 DGKα$^{-/-}$ mice). (D-I) B cells were allowed to settle on ICAM-1/CXCL13 planar lipid bilayers loaded with su-Ag (5 and 1 molec/μm^2) for 10 min, and then imaged. (D) DIC, IRM and fluorescence su-Ag images at the contact plane of representative IS-forming WT, DGKζ$^{-/-}$ and R59-treated B cells. (E) Frequencies of IS formation. (F) Values of contact area, (G) su-Ag central cluster area (cSMAC; left) and total su-Ag fluorescence (FL) (in arbitrary FL units, AU; right) for DGKζ$^{-/-}$ B cells with established IS compared to WT. (H-I) As in F, G, but for R59-treated B cells. Each dot in E represents a single image field, and in F-I a single cell. Data in E are the merge of three independent experiments (n = 3); data for a representative experiment are shown in F-G, H-I (n = 3). Scale bar, 2.5 μm. ****, p<0.0001 by two-tailed unpaired Student's t-test.

Figure S2. DGKα$^{-/-}$ B cells have no defects in IS formation. B cells were allowed to settle on ICAM-1/CXCL13 planar lipid bilayers loaded with su-Ag (20 molec/μm^2) for 10 min, and then imaged or fixed for immunofluorescence. (A) DIC, IRM and

fluorescence su-Ag images at the contact plane of representative IS-forming WT and DGKα$^{-/-}$ B cells. (B) Frequencies of IS formation. Values of (C) contact area, (D) su-Ag central cluster area (cSMAC; left) and total su-Ag fluorescence (FL) (in arbitrary FL units, AU; right) for DGKα$^{-/-}$ B cells with established IS compared to WT. Each dot in B represents a single image field, and in C, D a single cell. (E) DIC and FL images of F-actin (white) for representative IS-forming WT and DGKα$^{-/-}$ B cells. Right, values of total F-actin FL at the IS in each case. (F) As in E but of vinculin (green). Each dot in E and F is a single cell. Data in B are the merge of three independent experiments (n = 3); data for a representative experiment are shown in C to F (n = 4). Scale bar, 2.5 μm. Statistics analysis by two-tailed unpaired Student's t-test.

Figure S3. DGKζ overexpression enhanced LFA-1-mediated adhesion and vinculin/F-actin content at the A20 B cell synapse. Transfected A20 B cells were allowed to contact ICAM-1/CXCL13 planar lipid bilayers loaded with su-Ag (20 molec/μm^2) for 20 min, and then imaged or fixed for immunofluorescence. (A) Representative profiles of GFP, and of GFP-tagged DGKζ-WT and DGKζ-KD expression in transfected A20 B cells 20 h after electroporation; frequencies of GFP^{neg} (left bar) and GFP$^+$ (right bar) within transfected cells are indicated for each case. (B) Frequencies of IS formation for none transfected (GFP^{neg}; none) and GFP, DGKζ-WT and DGKζ-KD transfected A20 B cells. (C) DIC, IRM and fluorescence images of GFP and su-Ag at the contact plane of representative IS-forming transfected A20 B cells. Values of (D) contact area, (E) su-Ag central cluster area (cSMAC; left) and total su-Ag fluorescence (FL) (in arbitrary FL units, AU; right) for A20 B cells with established IS in each case. (F) DIC and FL images of F-actin (white) for representative IS-forming transfected A20 B cells. Left, values of total F-actin FL at the IS in each case. (G) As in

F, but for vinculin (green). Mid-graph, frequencies of well-formed vinculin rings for none transfected (GFP^{neg}; none) and DGKζ-WT and DGKζ-KD transfected A20 B cells in presence of distinct tethered su-Ag densities at the lipid bilayer. Right graph, values of total vinculin FL at the IS in each case. Data in B are the merge of three experiments (n = 3); data of a representative experiment are shown in D, E (n = 4); data in F, G, are the merge of two experiments (n = 3). Scale bar, 5 μm. *, p<0.05; **, p<0.01; ***, p<0.001; ****, p<0.0001 by two-tailed unpaired Student's t-test.

Figure S4. Addition of exogenous PA modifies the su-Ag central cluster at the B cell IS. B cells were in contact with ICAM-1/CXCL13 planar lipid bilayers loaded with su-Ag (20 molec/μm^2) for 10 min to establish the IS, imaged, then exposed to 0.1 mM PA (30 min) and imaged. (A) DIC and FL images of su-Ag for representative DGK$\zeta^{-/-}$ and WT B cells before (none) and after PA exposure. (B) Values su-Ag central cluster area (cSMAC; left) and total su-Ag fluorescence (FL) (in arbitrary FL units, AU; right) for each cell type and condition; each dot is a single cell. (C) Immunoblot of WT B cells non-treated (none) and PA-treated (0.1 mM) during 1 h in culture, probed with specified antibodies. Lysates from a representative mouse are shown. Right, Quantification of phosphorylated-PAK1 (p-PAK1) and p-PAK2 intensity normalized to loading control (α-Tubulin, α-Tub). Data of a representative experiment are shown in B (n = 4); data in C are the mean ±SD of three mice. Scale bar, 2.5 μm. *, p<0.05; **, p<0.01; ****, p<0.0001 by two-tailed unpaired Student's t-test.

Figure S5. DGKζ-derived PA in combination with PI3K-generated PIP_3 regulate F-actin polymerization at the B cell IS. (A) Immunoblot of WT, DGK$\zeta^{-/-}$ and R59-treated (R59) B cells stimulated on Ab-coated plates for the indicated times, probed with the

specified antibodies. Right, quantification of phosphorylated (S473) Akt (p-Akt) intensity normalized to α-Tubulin loading control (α-Tub). (B-G) B cells were allowed to settle on ICAM-1/CXCL13 planar lipid bilayers loaded with su-Ag (20 molec/μm^2) for 10 min, and then imaged. (B) DIC, IRM and su-Ag FL images for representative untreated (none) or LY-treated (LY) WT and DGK$\zeta^{-/-}$ B cells. Values of (C) contact area, (D) su-Ag central cluster area (left) and total su-Ag FL (in AU; right) for each B cell type in each case. (E) DIC, IRM and su-Ag FL images for representative untreated or R59-treated (R59) WT and PI3Kδ KD (KD) B cells. Values of (F) contact area, (I) su-Ag central cluster area (left) and total su-Ag FL (in AU; right) for each B cell type in each case. Data of a representative experiment are shown in C, D, F and G (n = 3); data in A are the mean ±SD of three experiments (n = 3). Scale bar, 2.5 μm. **, p<0.01; ****, p<0.0001 by two-tailed unpaired Student's t-test.

Figure S6. Traction Force Microscopy and Micropipette Force Probe experimental set up; phosphorylated ERK levels at the DGKα$^{-/-}$ B cell IS compared to WT. (A) Cartoon of TFM assays, showing B cells settled on fluorescent-microbeads-containing PAA gels loaded with su-Ag alone (left) or plus ICAM-1-Fc (right). Black arrows, cell direction forces; white arrows, microbeads displacement direction. (B) Scheme of the MFP set up. A stiff micropipette holds a cell with a gentle aspiration (typically 50 Pa) controlled by the height of a water reservoir (left), while a flexible micropipette holds an activating bead firmly aspirated through the use of a syringe filled with air (right). Both micropipettes have a 45° bend, so their tips are in the focal plane of the inverted microscope. Inset: zoom on the cell contacting the bead at the tip of the flexible micropipette. (C) During the experiment, the position of the center of the bead along the x-axis (X_{bead}) is tracked over time. The base of the flexible micropipette is controlled by

a piezo stage. Knowing both the bead position and the position of the flexible micropipette base allows calculating the deflection of the flexible micropipette, which once multiplied by the flexible micropipette stiffness is the force applied by the probe. An automated feedback loop acts on the position of the piezo stage in order to apply a controlled force to the cell; red dashed line, bead position (X_{bead}); black dashed line, zero value. (D) WT and DGK$\alpha^{-/-}$ B cells were in contact with ICAM-1/CXCL13 planar lipid bilayers loaded with su-Ag (20 molec/μm^2) for 10 min, and then fixed for immunofluorescence. Left, DIC and FL images of phosphorylated ERK1/2 (p-ERK; green) for representative IS-forming B cells. Right, values of total p-ERK FL at the IS in each case; each dot is a cell. Data of a representative experiment are shown (n = 4). Scale bar, 2.5 μm; statistics analysis by two-tailed unpaired Student's t-test.

Figure S7. Experimental set up for the evaluation of B cell antigen extraction and presentation to OTII CD4$^+$ T cells. (A) Left, scheme of *in vitro* B cell proliferation assays; right, gating strategy for proliferation analysis. (B) WT B cells were cultured in contact with ICAM-1/CXCL13 planar lipid bilayers, coated with Alexa Fluor 647-streptavidin (strep) and non-loaded (none) or loaded with su-Ag/OVA at specified densities (ranging from 20 to 2500 molec/μm^2), for 2 h. Then B cells were collected, treated with trypsin (5 min), and analyzed by flow cytometry for strep and OVA (Alexa Fluor 488-conjugated) fluorescence as readout of su-Ag/OVA extraction. Representative profiles of strep (top) and dot plots of strep/OVA (bottom) for each density are shown. (C) As in B, but in contact with su-Ag/OVA-loaded (2500 molec/μm^2) planar lipid bilayers in absence or presence of 0.1 mM PA for 2 h. Frequencies of strep$^+$ B cells (left) and mean fluorescence intensity (MFI) strep values (right) in presence of su-Ag/OVA for each condition. Data are the merge of three independent experiments (n = 5 mice). (D)

Left, scheme of *in vitro* antigen presentation assays; right, gating strategy for CD25 surface expression and proliferation analysis in $CD4^+$ OTII T cells. Statistics analysis by two-tailed unpaired Student's *t*-test.

Figure S8. Germinal center response of recipient $CD45.1^+$ B cells. (A) Gating strategies to analyze recipient $CD45.1^+$ B cells ($CD45.1^+$ $CD19^+$ or $CD45.1^+$ $B220^+$) in spleen. (B) Strategy to measure the frequencies of total GC ($GL7^+$ Fas^+) and NP-specific GC ($GL7^+$ Fas^+ IgD^{neg} NP^+) $CD45.1^+$ $B220^+$ B cells generated seven days after immunization with the T cell-dependent antigen NIP-OVA plus Alum; representative density plots of recipient B cells from mice adoptively transferred with $CD45.2^+$ WT (WT-transferred) or DGK$\zeta^{-/-}$ (DGK$\zeta^{-/-}$-transferred) B cells are shown. Frequencies of gated cells are indicated. (C) Frequencies of total GC B cells (left) and of NP-specific GC B cells (right) in the $CD45.1^+$ $B220^+$ B cell population at the spleens of each mice group; each dot is a mouse. (D) Representative density plots of plasma cell ($CD19^+$ $CD138^+$) and class-switched IgG1 B cell ($CD19^+$ $IgG1^+$) generation for recipient $CD45.1^+$ B cells in each case; frequencies of gated cells are indicated. (E) Frequencies of plasma cells and $IgG1^+$ B cells in the recipient $CD45.1^+$ $CD19^+$ B cell population at the spleens of each mice group; each dot is a mouse. Data in C, E, are the merge of two independent experiments ($n = 2$). Statistics analysis by two-tailed unpaired Student's *t*-test.

Figure S9. Model for DGKζ roles and lipid signaling interplay at the B cell immune synapse. (A) BCR recognition of antigen triggers PIP_3 production by PI3K. PIP_3 recruits Btk together with PIP5KI from the cytosol to the plasma membrane; PIP5KI produces PIP_2, substrate of PI3K and PLCγ2. Btk activates PLCγ2, which consumes PIP_2 to produce IP_3 and DAG. PIP_3 promotes actin polymerization by DOCK2 recruitment and

Rac activation, and PIP_2 supports vinculin/WASP translocation to the plasma membrane; these lipids participate of pSMAC assembly and antigen gathering. Related to canonical BCR signaling, IP_3 leads to Calcineurin/NFAT pathway activation through Ca^{2+} release from the endoplasmic reticulum followed by Ca^{2+} influx by store-operated channels (SOC). DAG promotes PKC/RasGRP activation and therefore the NFκB and ERK signaling cascades. All three pathways lead to gene transcription, B cell activation and proliferation. Classical PKC facilitates DGKζ activation and translocation to the plasma membrane by phosphorylation. (B) DGKζ consumes DAG to produce PA, limiting canonical BCR signaling (highlighted in red color), such as NKκB/ERK pathways and Ca^{2+} signaling amplification. DAG activates store-independent TRPC3 channels, which drive Ca^{2+} influx and PLCγ2 activation. Besides, DGKζ and its product PA support other important synapse-related events (highlighted in green color). They regulate pSMAC maintenance by two means. First, PA enhances PIP5KI activity, increasing PIP_2 production at the synapse and therefore vinculin-mediated pSMAC stabilization. Second, PA and DGKζ scaffold activity lead to Rac-mediated actin polymerization by keeping DOCK2 at the membrane and PAK/RhoGDI axis activation. DGKζ also governs MTOC polarization and mechanical force generation at the B cell synapse, both necessary for antigen acquisition. The molecular mechanism/s by which DGKζ regulates MTOC translocation in B cells requires further studies. DGKζ-mediated regulation of myosin-II activity, actin polymerization and LFA-1 adhesion may be involved in mechanical force generation.

SUPPLEMENTARY METHODS

K' parameter quantification

We link oscillatory force *F* and cell length *L* by using a complex formalism that is convenient to analyze in rheology experiments (1) and define a complex stiffness K^* to link the force $F = F_0 + \Delta F e^{i\omega t}$ and cell length $L = L_0 + \Delta L e^{i(\omega t - \varphi)}$ (here i is the complex imaginary square root of 1). The complex cell stiffness K^* is such that:

$$F - F_0 = K^*(L - L_0)\ (Eq.1).$$

As a complex quantity K^* can further be written as $K^* = K' + iK"$ where the real part K' quantifies the elastic properties of the cell, and the imaginary part $K"$ quantifies the viscous properties of the cell. By introducting the expression of F and L in equation 1, we obtain $\Delta F e^{i\omega t} = K^*\left(\Delta L e^{i(\omega t - \varphi)}\right)$, so that $K^* = \Delta F/\Delta L\, e^{i\varphi}$, from which we deduce that $K' = (\Delta F/\Delta L)\cos\varphi$ (Eq. 2) and $K'' = (\Delta F/\Delta L)\sin\varphi$ (Eq. 3). In this study, equation 2 is used to compute K' from the experimentally measured ΔF, ΔL, and φ. Note that the parameter K' is expressed in force per unit length and is not an intrinsic elastic modulus such as a Young's modulus that is expressed in Pa (force per unit area): K' depends on the geometry of the cell. Thus, a change in K' can be due to two different effects: a change in geometry of the cell (its length or surface area in contact with the bead) or a change in intrinsic mechanical properties of the cell. In this study, we did not go into this separation of both effects, but importantly B cells do not undergo as large geometrical changes as other leukocytes (T cells undergo much larger deformation upon activation (2)), so that as a first approximation considering that the geometry of the cell is not changing, observed changes in K' can be attributed to changes in intrinsic mechanical properties. A good indication that this approximation is valid is the fact that we observed activating cells that did spread much more that others that stayed relatively

round upon activation, while still showing a clear increase in K'. Furthermore, we also observed non-activating cells (using control beads, without su-Ag) that showed some relative changes in length, but these changes did not result in any increase in K'. These examples are given in the following Supplementary Figure 5.

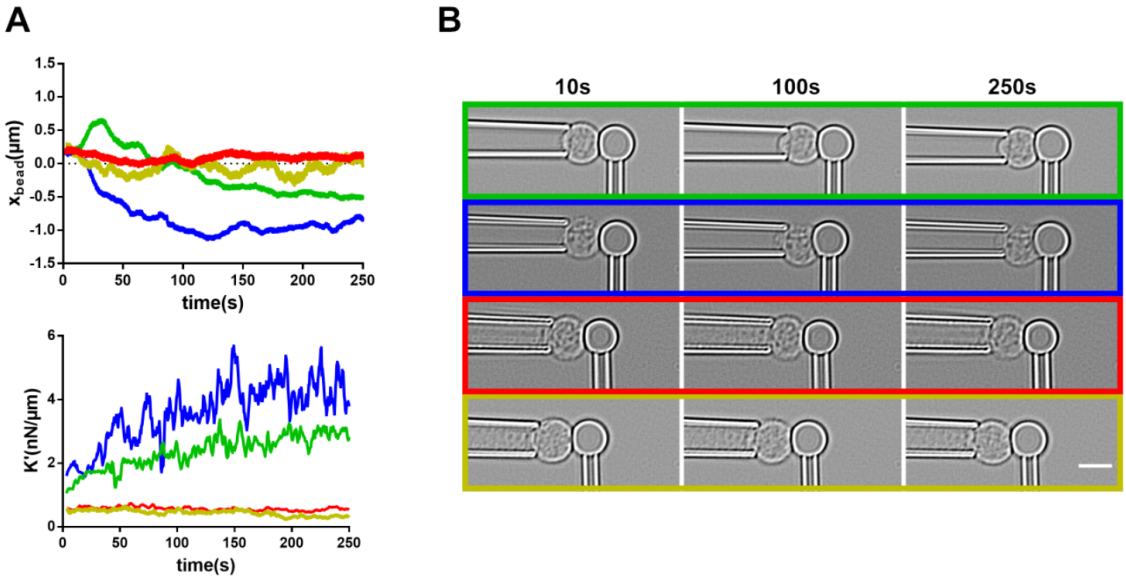

Supplementary Figure 5. Four examples of B cells showing that changes in cell shape and changes in the value of K' do not correlate. (A) X_{bead} and K' values over time. (B) Microscopy images of the corresponding B cells. Each color corresponds to a cell. Green: WT B cell that stays round during the experiment with su-Ag-containing bead. Blue: WT B cell that spreads on the su-Ag-containing bead during the experiment. Both activating cells lead to an increase in K' with similar dynamics. Red: WT B cell that stays round and does not show any change in K' (control bead). Yellow: WT B cell that fluctuates slightly in shape (see yellow X_{bead} trace) but does not show any increase in K'.

Supplementary References

1. Fabry B, *et al.* (2001) Scaling the microrheology of living cells. *Phys Rev Lett* 87(14):148102.

2. Sawicka A, *et al.* (2017) Micropipette force probe to quantify single-cell force generation: application to T-cell activation. *Mol Biol Cell* 28(23):3229-3239.

SUPPLEMENTARY MOVIE LEGENDS

Movie 1. Stress maps generated by WT B cells contacting su-Ag coated substrates (polyacrylamide gels); a representative cell is shown. Movie is generated after analysis of beads displacement using traction force microscopy inversion algorithm. One image every 5 sec.

Movie 2. Stress maps generated by DGK$\zeta^{-/-}$ B cells contacting su-Ag coated substrates (polyacrylamide gels); a representative cell is shown. Movie is generated after analysis of beads displacement using traction force microscopy inversion algorithm. One image every 5 sec.

Movie 3. Stress maps generated by WT B cells contacting su-Ag/ICAM-1-Fc coated substrates (polyacrylamide gels); a representative cell is shown. Movie is generated after analysis of beads displacement using traction force microscopy inversion algorithm. One image every 5 sec.

Movie 4. Stress maps generated by DGK$\zeta^{-/-}$ B cells contacting su-Ag/ICAM-1-Fc coated substrates (polyacrylamide gels); a representative cell is shown. Movie is generated after analysis of beads displacement using traction force microscopy inversion algorithm. One image every 5 sec.

Movie 5. Micropipette Force Probe assay, related to Figure 3. Bright field video shows a WT B cell (left) contacting with an ICAM-1-containing lipid-coated silica bead without su-Ag (right). Time displayed in the top left corner of the video.

Movie 6. Micropipette Force Probe assay, related to Figure 3. Bright field video shows a WT B cell (left) contacting with an ICAM-1-containing lipid-coated silica bead with tethered su-Ag (right). Time displayed in the top left corner of the video.

Movie 7. Micropipette Force Probe assay, related to Figure 3. Bright field video shows a DGK$\zeta^{-/-}$ B cell (left) contacting with an ICAM-1-containing lipid-coated silica bead with tethered su-Ag (right). Time displayed in the top left corner of the video.

Movie 8. Micropipette Force Probe assay, related to Figure 3. Bright field video shows a WT R59-treated B cell (left) contacting with an ICAM-1-containing lipid-coated silica bead with tethered su-Ag (right). Time displayed in the top left corner of the video.

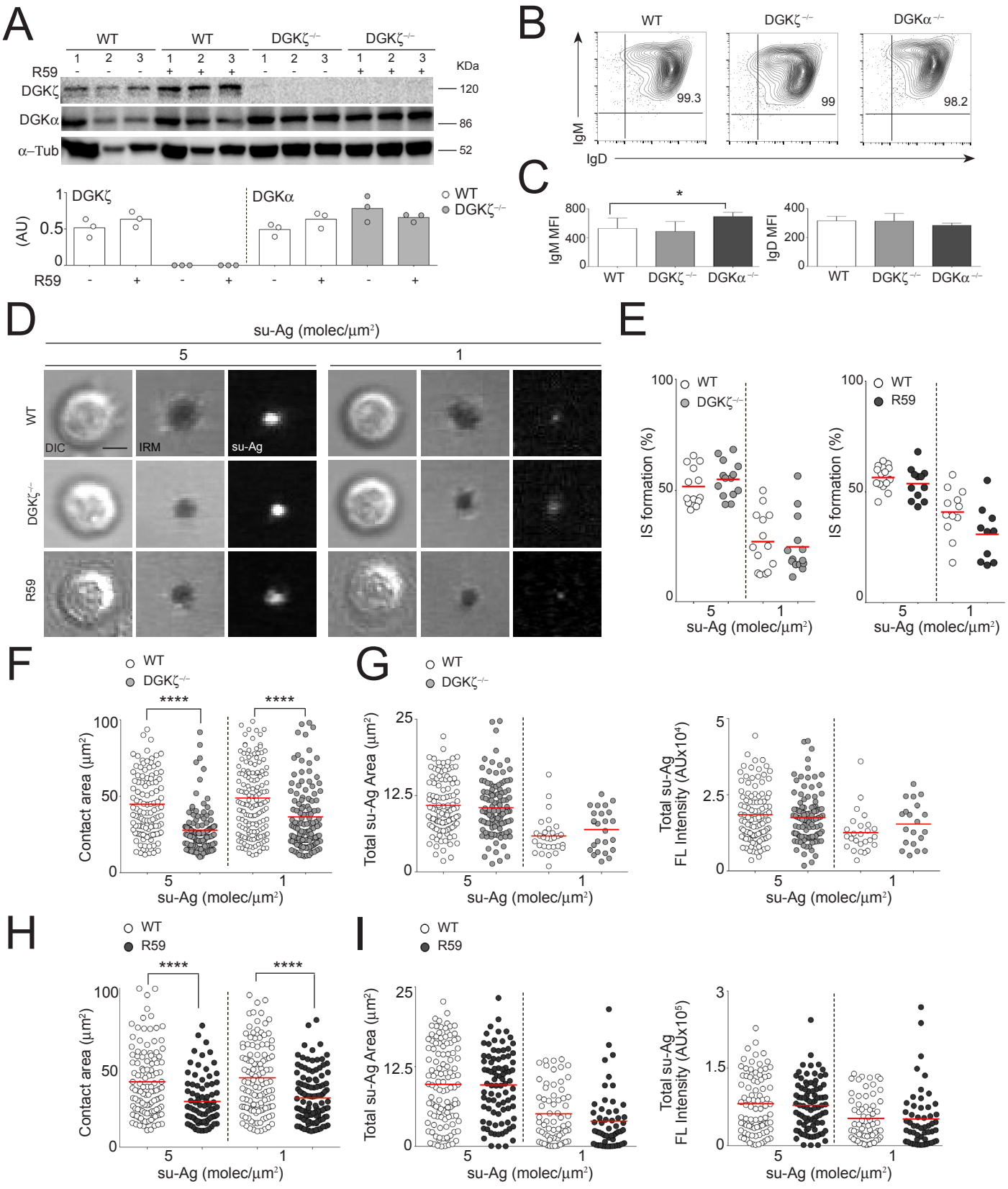

Figure S1. Merino-Cortés *et al.*

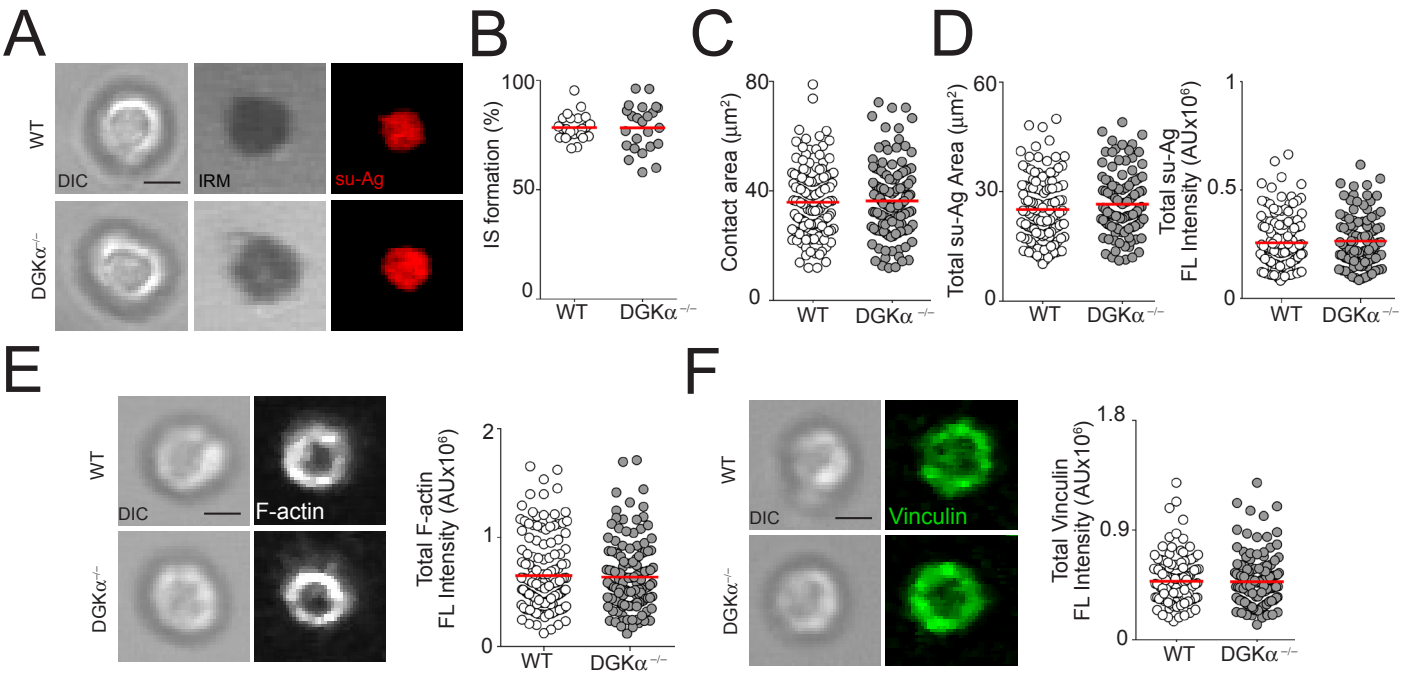

Figure S2. Merino-Cortés *et al.*

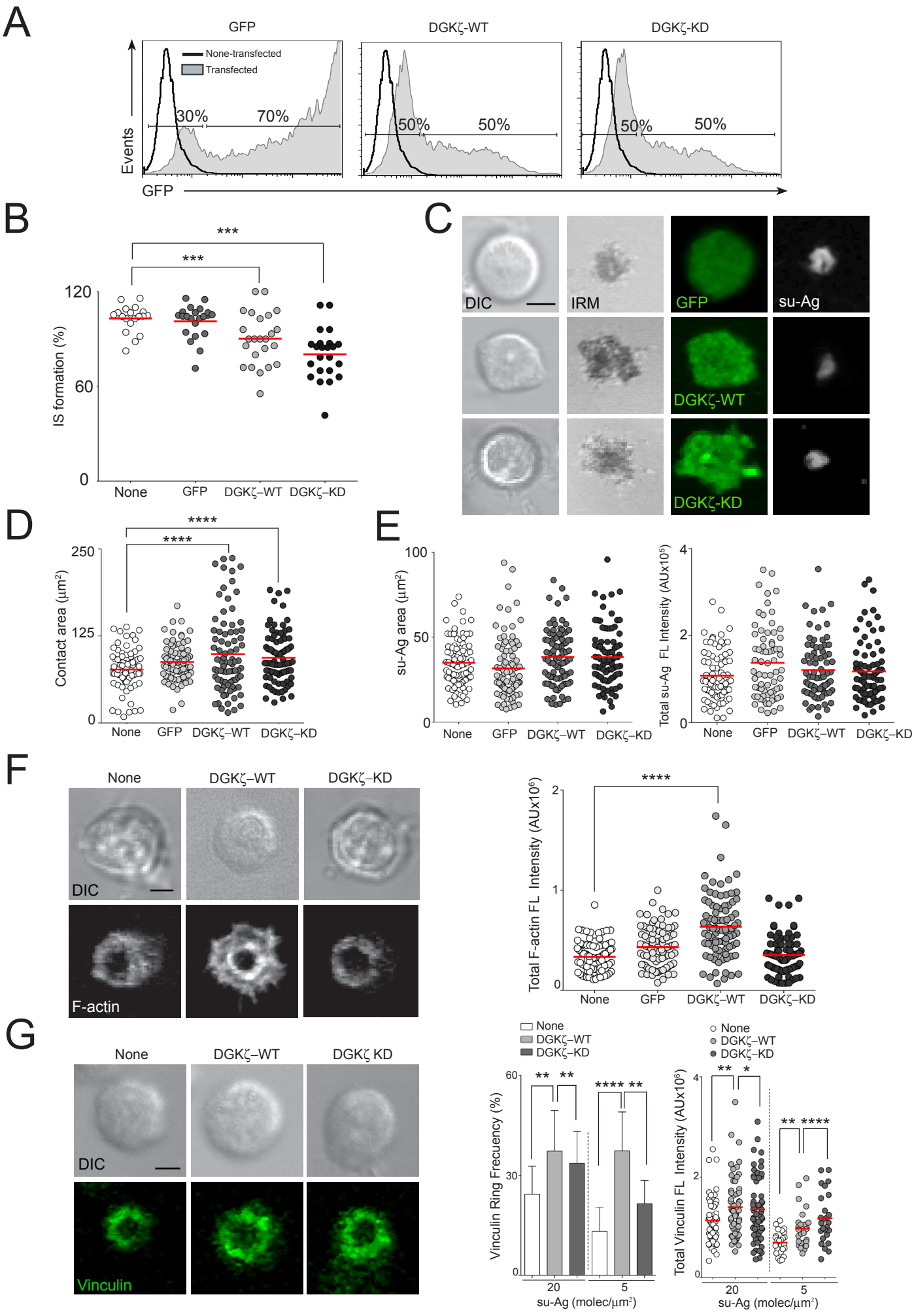

Figure S3. Merino-Cortés *et al.*

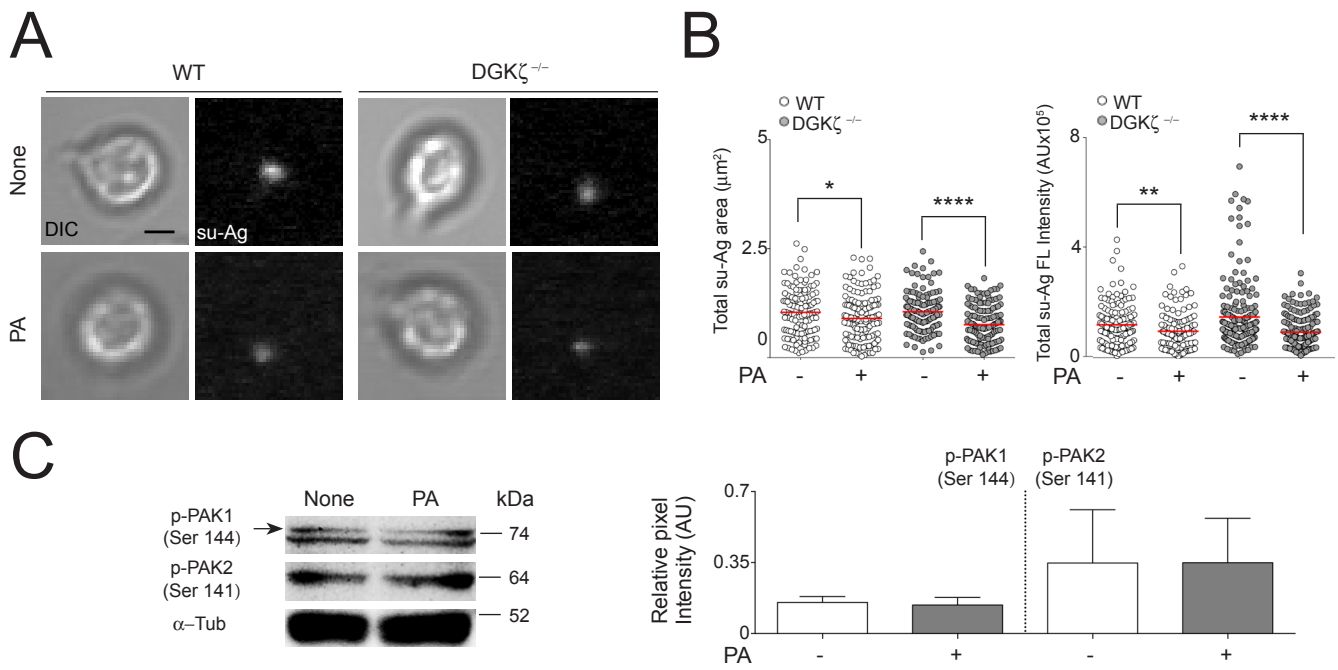

Figure S4. Merino-Cortés *et al.*

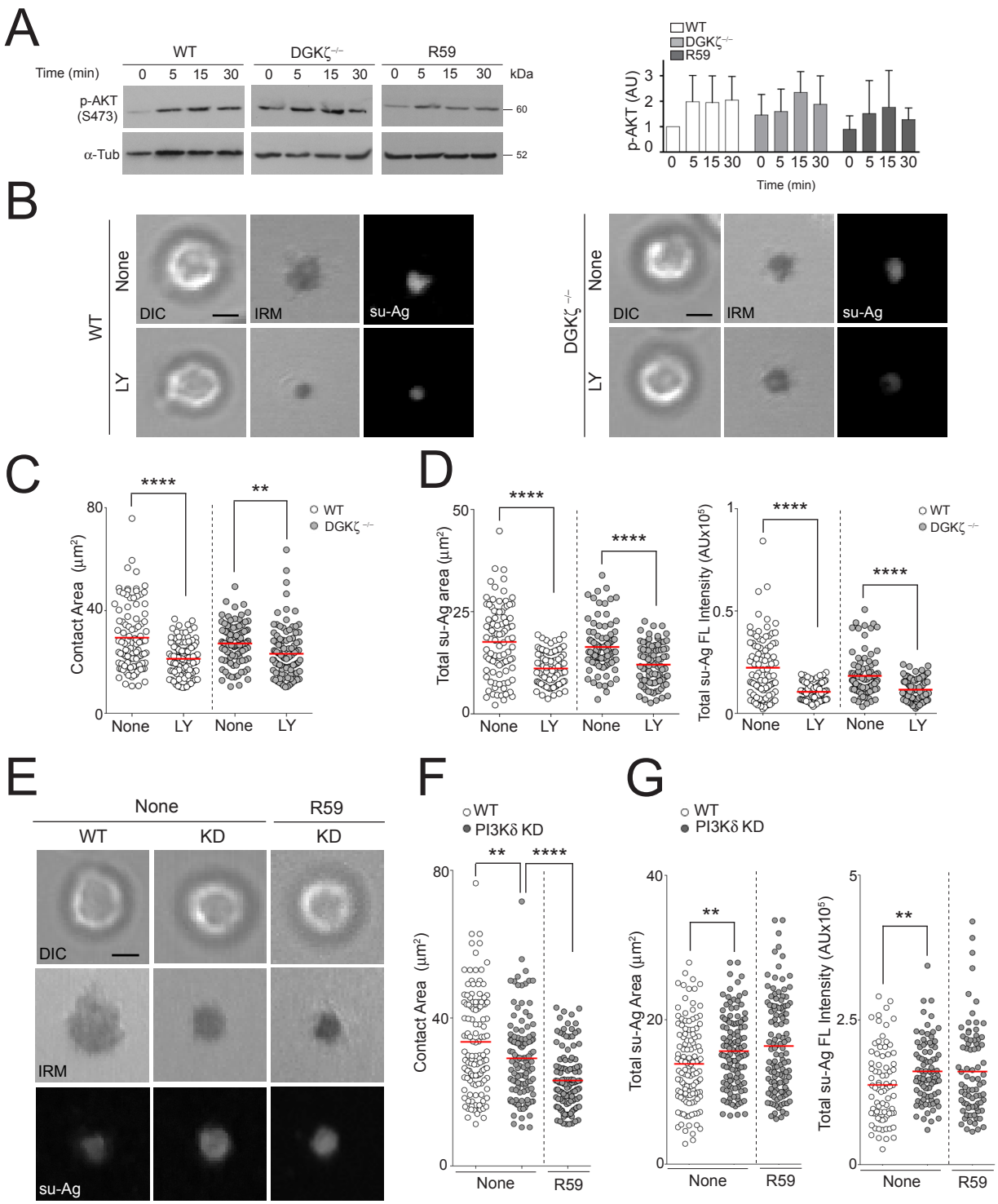

Figure S5. Merino-Cortés *et al.*

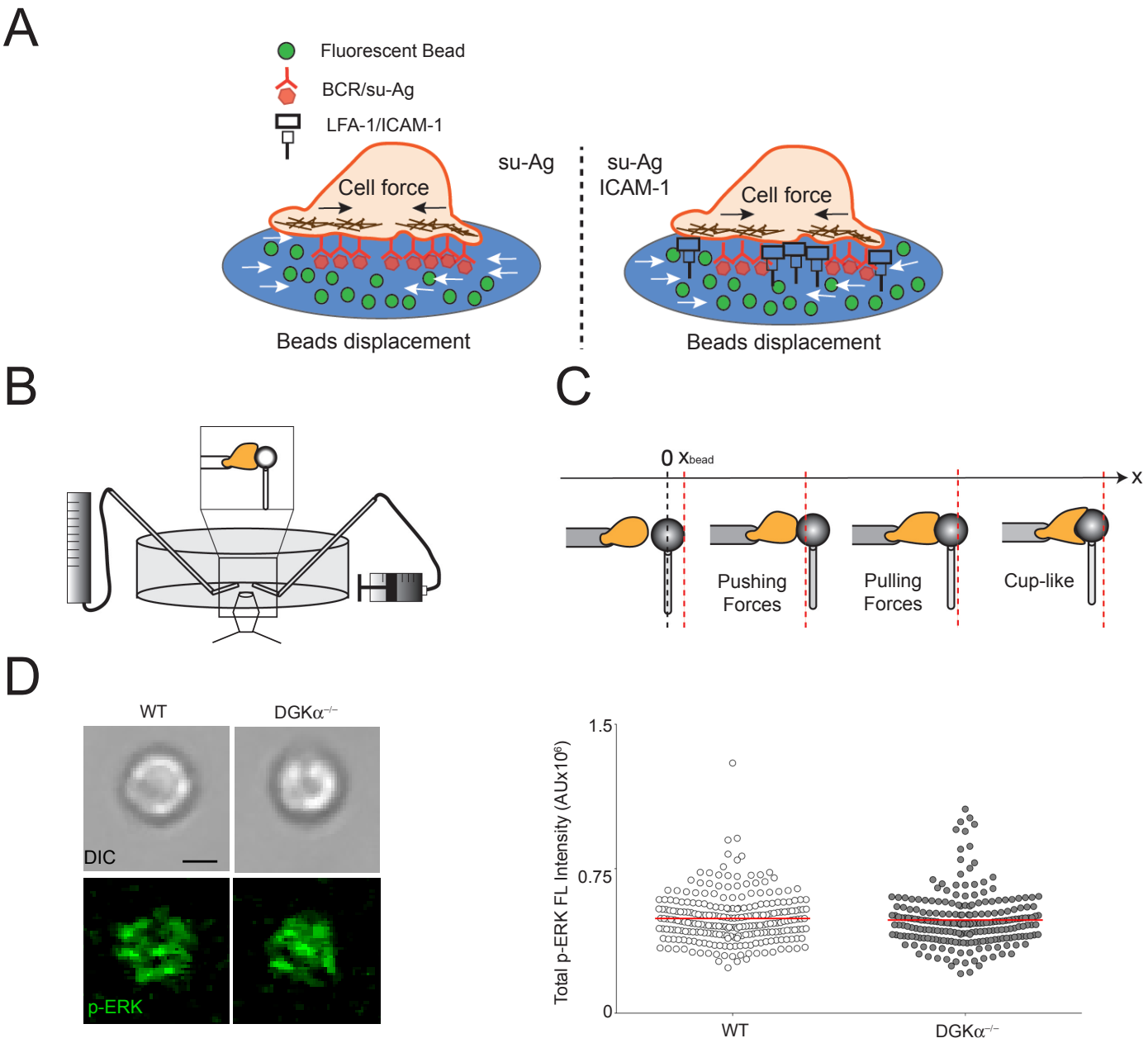

Figure S6. Merino-Cortés *et al.*

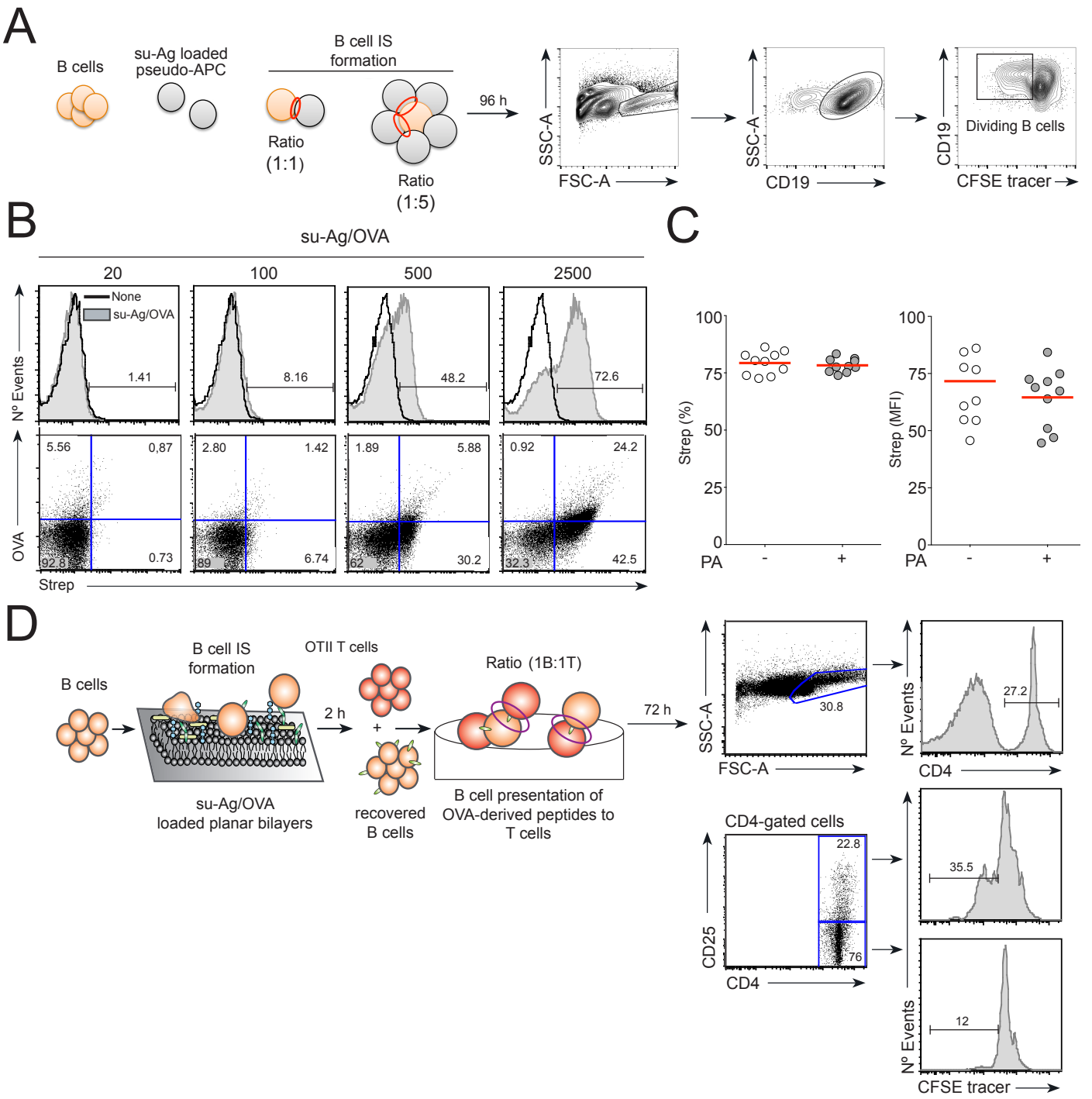

Figure S7. Merino-Cortés *et al.*

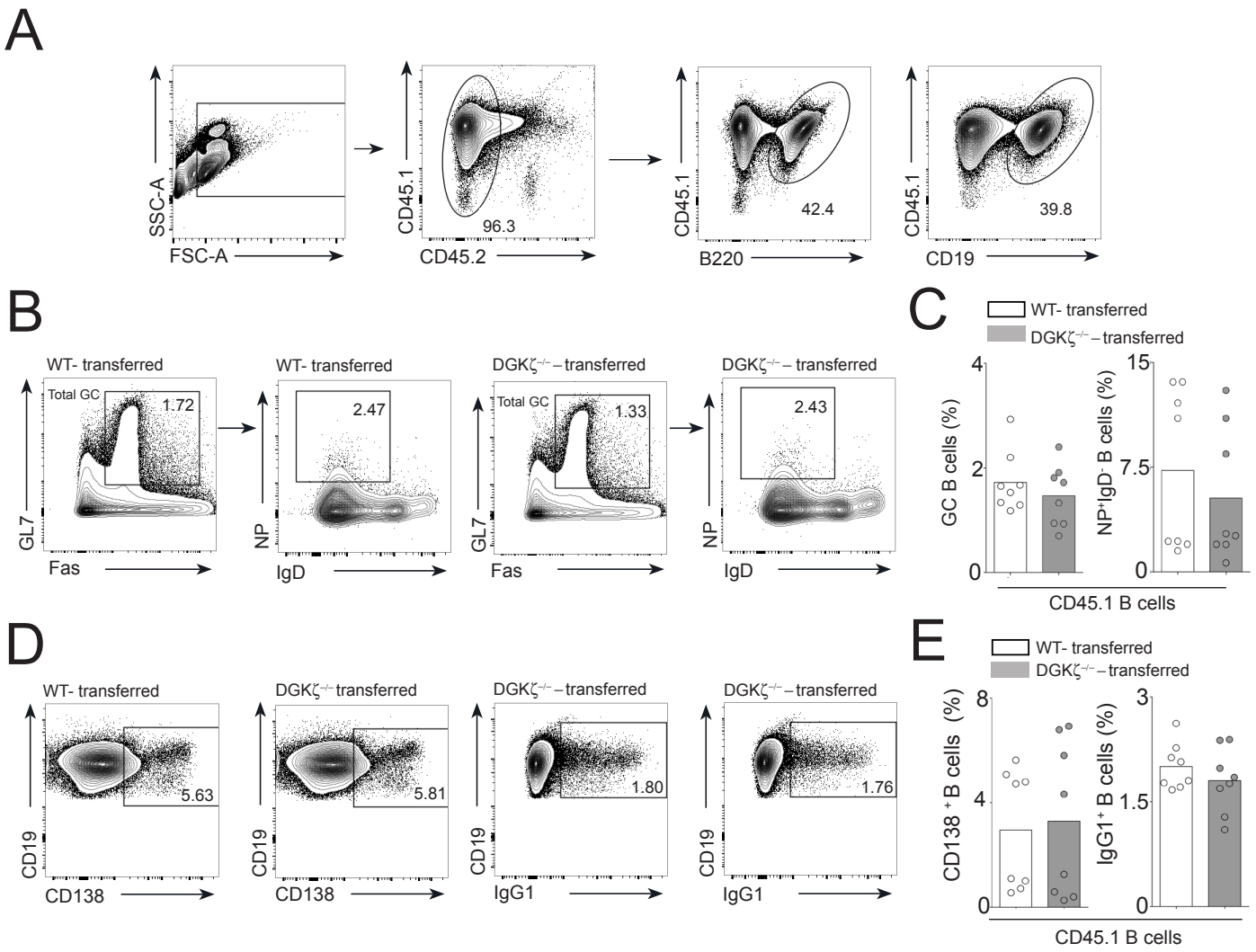

Figure S8. Merino-Cortés *et al.*

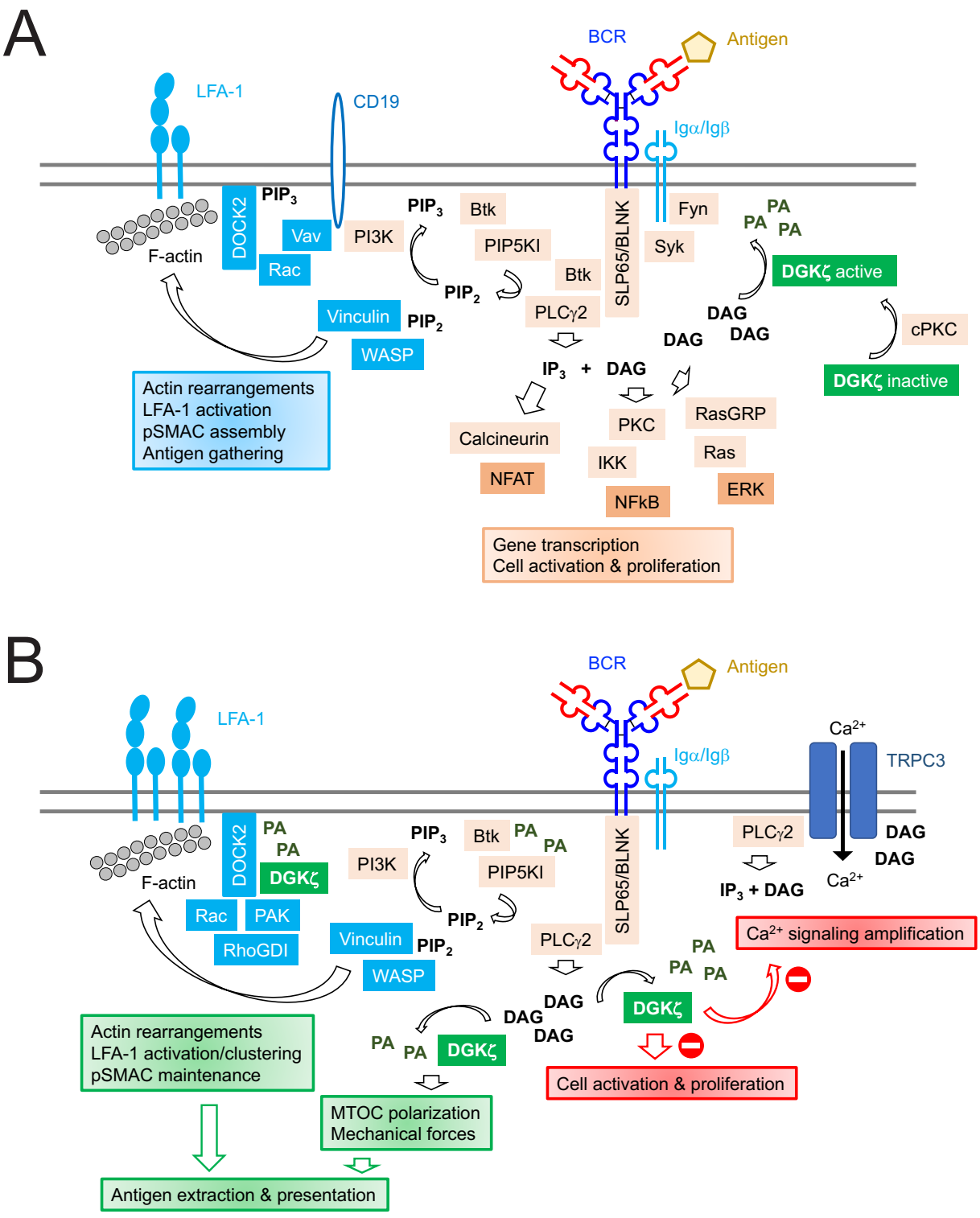

Figure S9. Merino-Cortés *et al.*